Veikka Nikander

NUMERICAL FRONT CONTACT GRID OPTIMIZATION FOR PHOTOVOLTAICS
Theory and simulations

TIIVISTELMÄ

Veikka Nikander: Valojännitekennon etukontaktikuvioinnin numeerinen optimointi
Diplomityö
Tampereen yliopisto
Teknis-luonnontieteellinen
Huhtikuu 2023

Valojännitemuuntimet ovat tärkeä osa energiaa valosta -teknologiaa, jossa energiaa siirretään valon avulla, perinteisen sähköjohteen tai induktion sijaan. Valosta energiaa -järjestelmiä käytetään kun tarvitaan energian siirtolinja, joka on galvaanisesti erotettu, immuuni sähkömagneettiselle häiriölle tai kun halutaan ultrakevyitä siirtolinjoja. Tehotiheys on valojännitemuuntimen avainsuoritusparametri. Kuitenkin siirryttäessä korkeisiin tehotiheyksiin, kaksi rajoittavaa häviömekanismia alkavat rajoittaa kennon toimintaa: lämpenemisestä johtuva tehon alenema sekä vastushäviö. Valojännitekennoissa yleinen tapa vähentää vastushäviöitä on valmistaa kennon etupintaan metallikuviointi, joka avustaa virran siirtymistä sivuttaissuunnassa.

Numeerinen etumetalloinnin optimointi suoritettiin kahdelle yksiliitosvalojännitemuuntimelle uudella *Hybrid quasi-3D* simulaatiomallilla. Malli rakennettiin olemassa olevista optisista sekä puolijohdefysiikan simulaatiomalleista, tehden mallista luotettavan ja tarkan kuvauksen valojännitemuuntimesta. Kahden kokoojakiskon tasasormikuviointi optimoitiin kahdelle samantyyppiselle sirulle, josta toinen oli p–n polaarinen (p-tyyppinen puolijohde n-tyyppisen päällä) ja toinen n–p tyyppinen diodirakenne. Optimointi tehtiin neljälle sädemuodolle sekä kolmelle käyttölämpötilalle, jotta saataisiin mahdollisimman kattava kuva rakenteiden eroista sekä etumetalloinnin määrästä. Lisäksi kennon avoimen piirin jännitettä, suljetun piirin virtaa sekä täytekerrointa (fill factor) analysointiin syvemmän ymmärryksen saavuttamiseksi kennon toiminnasta eri olosuhteissa.

Tulosten perusteella n–p diodirakenne on huomattavasti parempi korkean tehotiheyden käyttöalueella verrattuna p–n rakenteeseen. N–p rakenteen sormien välitys oli tuplasti suurempi ja ulostuloteho 8,5-9,6 % suurempi kuin p–n rakenteella. Sormien välityksen toleranssi oli myös huomattavasti suurempi n–p rakenteella. Säteen muodon epätasaisuus sekä kennon käyttölämpötilan kasvu molemmat kavensivat optimaalista sormien välitystä. Säteen muoto vaikutti sormien välityksen kaventumiseen enemmän. Molemmat tekijät kavensivat myös sormien välityksen toleransseja. Täytekertoimen analyysin perusteella p–n rakenteen emitterimateriaalin, p-tyyppisen galliumarsenidin, matala enemmistövarauksenkuljettajien liikkuvuus ja sen aiheuttama korkea neliöalan resistanssi rajoittavat rakenteen toimintaa suurilla sormien välityksillä. Mielenkiintoinen lisätulos oli myös havainto avoimen piirin jännitteen pienenemisestä sormivälityksen kasvaessa. Tulos voitiin selittää ajatuskokeella eri jännitteisten jännitelähteiden yrityksenä tasata järjestelmän kokonaisjännite.

Hybrid quasi-3D malli osoittautui käyttökelpoiseksi malliksi valojännitekennojen mallintamiseen. Tehokas 3D malli on arvokas työkalu valojännitesirukehittäjälle, joka haluaa laajentaa 1D puolijohdekerrosten kehityksestä kehitystyötä laajemmalle moduulitasolle. Kyky mallintaa puolijohdekerrosrakenteita, valon säteen profiileita sekä etumetallointia yhdessä mallissa antaa kyvyn rakentaa maailmanluokan valojännitekennoja ja täten menestyä kovan kilpailun valojännitekennojen alalla.

Avainsanat: valojännitekenno, numeerinen optimointi, etukontaktimetallointi

ABSTRACT

Photovoltaic converters are a key part of the power by light systems, which transfer energy via light rather than electrical conduction or induction. They excel in applications requiring galvanic isolation, electromagnetic interference-free operation, and ultra-lightweight transmission lines. Power density is a key performance indicator for any photovoltaic chip, but this is even more true for the photovoltaic converter. Two main loss mechanisms start to play a limiting role as higher power densities are used: heating-related power loss and resistive losses. A common way to tackle the resistive loss of photovoltaic devices is to introduce front contact metallization on top of the chip to aid in the charge carrier transport at the lateral direction of the cell.

Numerical front contact grid optimization for two single junction photovoltaic converters is done with a novel Hybrid quasi-3D simulation model. The model is constructed by a collection of established optical and semiconductor simulation models giving an efficient yet reliable and accurate description of the photovoltaic device. Double busbar finger grid design's finger spacing is optimized for a similar but inverted p-type on n-type (p–n) and n-type on p-type (n–p) structures. Optimization is done for four relevant illumination profiles and three operation temperatures, to yield a comprehensive picture of the behavior between the two structures and different grid spacings. Analysis of the photovoltaic cell performance parameters V_{oc}, I_{sc}, and FF is done the gain a deeper knowledge of the cell behavior.

Results predict that the n–p structure performs considerably better at high illumination power compared to its p–n counterpart. The n–p structure yielded twice as large spacings and 8.5-9.6% higher output powers. Tolerance to spacing values was also considerably higher for n–p structures than p–n. Both illumination non-uniformity and temperature were found to decrease the optimal spacing values, with illumination having a stronger negative effect. Non-uniform illumination and temperature also had a negative effect on the spacing tolerance. Analysis of FF values revealed that with p–n structure, the device's low sheet resistance of the p-GaAs emitter starts to limit the cell performance as wider spacings are used. Also, results predicted V_{oc} values to decrease with increased spacing with non-uniform illumination. This effect was explained by a thought experiment of a voltage source matrix with non-uniform voltages trying to equalize their potential difference.

The Hybrid quasi-3D model proved to be a highly useful tool for simulating photovoltaic devices. The efficient 3D model has high value when the chip designer wants to move beyond the 1D layer level design to chip and module level design. The ability to consider the layer structure, illumination profile, and metal grid designs in the same model, gives the designer access to results needed to create world-class photovoltaics and to strive in the highly competitive industry of photovoltaics.

Keywords: photovoltaics, numerical optimization, front contact metallization

PREFACE

The work of this thesis has been carried out at the world-renowned Optoelectronics Research Center (ORC), Tampere University. As for a center in semiconductor and optoelectronics research and commercialization, I have been privileged to conduct my thesis work in this environment of cutting-edge technology. Experience and knowledge much wider than the scope of this work have been accumulated through interactions with colleagues holding both deep and wide knowledge in the aforementioned fields.

I would like to direct special thanks to Dr. Antti Tukiainen, who taught a young bachelor's student all the intricate knowledge of the basics of semiconductor physics and its application in photovoltaics. I would also want to thank Dr. Arto Aho for directing this knowledge in the research and development of novel photovoltaic cells as a role of the project manager of various photovoltaic research projects such as the European Research Council's project Ametist. Humble thanks are also in place for the whole solar cell team of ORC doing the real work in fabricating our photovoltaic devices and conducting the experiments on these devices. Lastly, I want to thank the ORC group leader, Prof. Mircea Guina for being a mentor and pushing me to excel in my work at the research group.

Studies in the former Tampere University of Technology and today's Tampere University has been challenging but balanced. I'm grateful for the friends I have made throughout my studies, the top-notch education, and for the possibility to attend an exchange period at Kobe University, Japan.

Last thanks I will direct to my family whom I can always trust with my cheers and falls.

Tampere, 26.4.2023

Veikka Nikander

CONTENTS

LIST OF ABBREVIATIONS AND SYMBOLS

As	arsenic
CC	Creative Commons license
DDM	double diode model
EHP	electron hole pair
Ga	gallium
GaAs	gallium arsenide
Ge	germanium
HQ3D model	Hybrid quasi-3D model
I–V	current–voltage
KPI	key performance indicator
PbL	power by light
PDD model	Poisson-drift-diffusion model
PV	photovoltaic
Si	silicon
SPICE	simulation program with integrated circuit emphasis
TMM	Transfer matrix method

$\vec{E}$	electric field
E_C	conduction band
E_F	Fermi energy
E_V	valence band
$E_{g,0}$	band gap at 0 K
E_g	band gap
E_i	middle energy of band gap
I_0	reverse voltage current
I_{mpp}	maximum power point current
I_{ph}	photogenerated current
I_{sc}	short circuit current
J^{diff}	diffusion current density
J^{drift}	drift current density
J_n	electron current density
J_p	hole current density
N_a	acceptor doping concentration
N_d	donor doping concentration
P_{mpp}	maximum power point power
R_e	recombination rate
R_s	series resistance
R_{sh}	shunt resistance
R_{sheet}	sheet resistance
V_0	bias voltage
V_{mpp}	maximum power point voltage
V_{oc}	open circuit voltage
n_e	electron concentration
n_i	intrinsic carrier concentration
w_0	beam waist at focus point
$\vec{x}$	space vector
ψ_k	wave function

Symbol	Description
ξ	recombination dependent coefficient for V_{oc} temperature dependency
E	electron energy
F	electric field
FF	fill factor
G	generation rate of photogenerated charge carriers
I	current
Irr_{max}	maximum irradiance
Irr	irradiance distribution
J	current density
P	power
R	reflectance
R	resistance
T	temperature
T	transmittance
U	Bloch function
V	bias voltage
W	Lambert W-function
d	semiconductor layer thickness
f	Fermi-Dirac probability function
g	Gaussian order
k	Boltzmann's constant
n	refractive index
p	hole concentration
q	elementary charge
t	time
w	beam waist of Gaussian beam
x	semiconductor layer depth
z	distance of focus point of gaussian beam
$\boldsymbol{k}$	momentum vector
β	phase shift
θ	angle of incidence
λ	wavelength
μ	charge carrier mobility
ω	angular frequency
ϵ	electromagnetic permittivity
ϕ	electric potential

1. INTRODUCTION

Solar cells are one of the important devices of the ongoing green energy transition and the battle against climate change. The technology maturity and consequent commercial deployment have been fast for the whole start of the millennia (IEA-PVPS, 2022; Luque & Hegedus, 2010). Constituting for 1002.9 TW or 3.6 % global annual electricity production as for the year 2021 (IEA, 2022), solar cells can be noted as one cornerstone of modern sustainable society.

Solar cells are a subclass of photovoltaic (PV) devices, which produce electrical power out of sunlight. Whereas solar cells are PV cells engineered to convert sunlight to electricity, other PV solutions exist for other light sources, such as ambient light (Bouclé et al., 2023) and thermal radiation (Datas et al., 2022). One PV application that has drawn attention lately is a PV converter, sometimes referred to as a PV laser converter or PV power converter. This PV device is optimized to convert monochromatic light coming from sources such as LED or laser, to electricity. These PV converters are an integral part of the power by light (PbL) technology.

In PbL technology, energy is transferred via artificial light instead of traditional forms of conduction and induction of electricity. Laser or LED transmitters are used for the conversion of electrical power to optical power, which is then transferred via optical fiber or free space to a receiver unit. At the receiver unit, the PV converter transfers the photonic energy stream back to electricity. While not as efficient as electrical wires in regular use at short to medium distances, PbL lines excel in applications requiring galvanic isolation (De Nazaré & Werneck, 2012), interference-free transmission and spark-free operation, to name a few. Other advantages compared to copper wires are a better weight-to-transferred-energy ratio for long-distance energy transfer lines and the option to use existing optical fiber infrastructure to transfer energy.

The conversion efficiency of solar cells is often *the* key performance indicator (KPI). The same applies to PV converters, but not with the same underline. With PV converters perhaps equally important KPI is the power density and output power of a given cell. Increased power density has benefits for three integral parts of any device performance: technical, economical and sustainability performance. For technical performance, the PV theory predicts that increased power density increases the efficiency of the device to an

extent (Luque & Hegedus, 2010). For economic performance, increased power densities decrease the required cell area of the device, yielding more devices from the same wafer. The same effect also contributes to the sustainability performance, since less rare materials such as gallium are used for the fabrication of devices.

However, when increasing the power density, two main loss mechanisms start to limit the performance: resistive losses and increased device temperature due to excess heat generation. Delicate thermal management can be deployed to tackle the temperature increase of the cell. Resistive losses on the other hand can be minimized by enhancing the conductivity of the charge carriers inside the device.

Front contact metallization is a common way to enhance the conductivity of the device and thus minimize the resistive losses since metals have higher conductivities than semiconductors used in PV cells (Lide, 1997; Sze & Irvin, 1968). The added front contact metal has one drawback, it shadows the underlaying active material, preventing the metallized part to absorb the coming light. Thus, we have an optimization problem, where for a given semiconductor structure, irradiance, and illumination profile one must find the optimal metal plating pattern to minimize the resistive losses and the shading losses.

In this thesis, a double busbar finger grid metallization is optimized for two III-V compound semiconductor single-junction PV converter designs. These designs are similar but inverted p-type on n-type and n-type on p-type structures, as short p–n and n–p structures. This simulation work is done with established tools of PV science and engineering, packed in a Python-based simulation library, Solcore (Alonso-Álvarez et al., 2018). A novel combination of these tools is utilized to achieve an efficient and accurate depiction of the simulated device, which the author has named a Hybrid Quasi-3D model. The work of this thesis was also published in a journal published by Springer, *Optical and Quantum Electronics* (Nikander et al., 2021).

The second chapter introduces the reader to the theory of semiconductors, p–n junctions, and photovoltaics giving an overview of the topic and a solid basis to understand the context of this work. The third chapter describes the theoretical models used in the simulation model by reviewing the different models used in the Hybrid quasi-3D model and concludes by describing how the model is constructed. In the fourth chapter, a grid optimization study is done with the Hybrid quasi-3D model for two opposite polarity single junction photovoltaic converter designs for three different operating temperatures and four illumination profiles. These results are analysed in chapter five and the sixth chapter wraps up the thesis by presenting the conclusions.

2. PHOTOVOLTAIC CELL

Photovoltaic (PV) cells can be realized with various types of materials. Historically silicon and III-V compound semiconductors have been the defacto materials for realizing these devices but emerging material choices of organic (Ameri et al., 2013; Riede et al., 2021; Tong et al., 2020) and perovskite (Gonzalez-Pedro et al., 2014; Jošt et al., 2020; Wang et al., 2016) are catching up in terms of conversion efficiencies. Regardless of this technological development, III-V semiconductor PV cells are still performing the best in terms of key features such as conversion efficiency (Geisz et al., 2020; Green et al., 2021) and especially in device lifetimes. Thus, the research and development of the established III-V semiconductor photovoltaics is still a key operation in the Optoelectronics research center and the focus of this thesis. It is to be noted that the tools, work, and results of this thesis can still be applied in the PV space outside III-V semiconductors, namely above mentioned organic and perovskite technologies.

We build our III-V semiconductor PV cell crystals layer-by-layer by using precisely controlled atom and molecular fluxes. Similarly, it is required to understand the physics of photovoltaics from building knowledge from atoms to semiconductor lattices and finally to the device level. In this chapter, we do exactly this.

2.1 Semiconductors

Atoms seek to gain a stabile, low-energy state by filling their outer, *valence*, shell with electrons. Most chemical elements from groups II-VII of the periodic table seek to fill their valence electron shell with eight electrons to form a so-called *octet*. For group IV atoms such as silicon (Si) or germanium (Ge), one way to achieve octet is by borrowing one electron from four other group IV atoms to form a *diamond lattice*. Participating atoms form a covalent bond with four neighboring atoms sharing one atom pair each, satisfying the octet. The same result can be achieved by combining equal amount of group III and group V atoms, like gallium (Ga) and arsenic (As), to form a compound III-V semiconductor: gallium arsenide (GaAs). This also holds true for II and VI group atoms like cadmium and tellurium. (Streetman & Banerjee, 2015)

Interesting behavior with atom orbitals can be observed when these atoms are brought to their distances formed by the created lattice: Individual atom states are "crammed" on top of each other, and quasi-continuous bands of available states are formed. This is visualized in Figure 1. For an ideal semiconductor at 0 K, all the electrons of the lattice

are occupied in a band consisting of bound states of atoms at the former valence orbital. This band is consequently called the valence band (E_V). If an electron gets sufficient energy to be excited to the higher band, it is relatively free to move around the lattice and can contribute to the conductivity of the material, giving the band name conduction band (E_C). The separation energy between these two energy bands is called band gap (E_g). E_g is a parameter of high importance with optoelectronic devices since it dictates photons emission and absorption wavelengths of the given material. (Streetman & Banerjee, 2015)
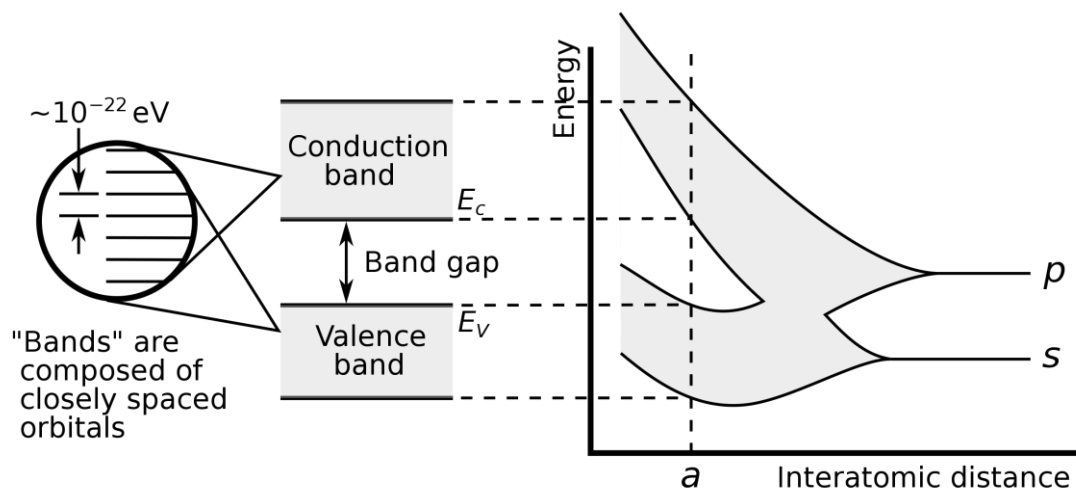
Figure 1. Formation of energy bands from individual atomic states. (Chetvorno, 2017) *Use under CC0.*

A more complete picture of the semiconductor band structures can be derived from the description of electron movement through the periodic semiconductor lattice. Electron is represented with Schrödinger's wave formalism, as a plane wave, through the periodically changing lattice with a wave function of

$$\psi_{\boldsymbol{k}} = U(\boldsymbol{k}, \vec{x})e^{ik\vec{x}}, \tag{1}$$

where $U(\boldsymbol{k}, \vec{x})$ is a Bloch function describing the allowed states at the lattice, $\boldsymbol{k}$ is the momentum vector and $\vec{x}$ space vector of the electron. With wave formalism, the energy bands can be described in the momentum space of the electrons. Depending on the momentum vector direction, the lattice periodicity seen by the electron changes and the energy bands change accordingly. Thus, energy bands need to be plotted for multiple lattice directions. (Streetman & Banerjee, 2015)

Two types of band gaps exist: direct and indirect. In materials with a direct band gap, the conduction band minima and the valence band maxima are at the $\boldsymbol{k} = 0$, whereas indirect semiconductors have the conduction band minima and the valence band maxima at different $\boldsymbol{k}$ values. Figure 2 shows examples for energy bands for direct and indirect

semiconductors. Examples of direct band gap semiconductors are for example gallium arsenide, indium gallium arsenide and gallium nitride and for indirect are silicon, aluminum arsenide and germanium.
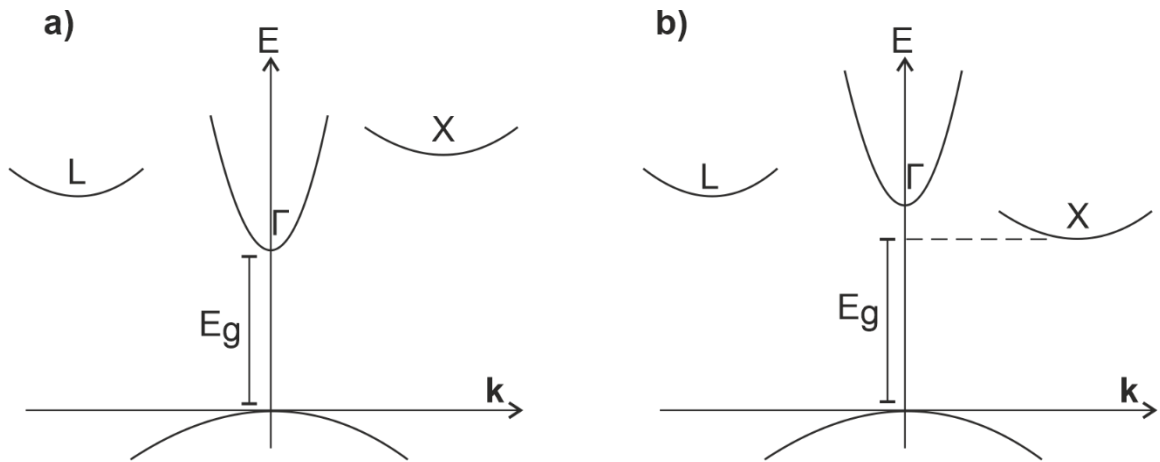

Figure 2 *Semiconductor band diagrams at **k** space for (a) direct and (b) indirect band gap semiconductor for three different lattice directions of Γ (**k**=0), X and L. Adapted from* (Streetman & Banerjee, 2015).

When an electron is excited from the E_V to E_C, a vacancy of available state is left behind to the E_V. This vacancy is called a *hole*, and the combination of excited electron and hole is called electron-hole pair (EHP). Electrons in the E_V are now available to move to the empty vacancy, hole, which consequently moves based on the electron movement (electron filling the hole leaves another hole behind). In effect, net movement of electrons is now possible on the valence band due to the hole and net charge can flow through the band. This flow of electrons can be modelled with the movement of holes, which is analogous to a positive charge moving at the valence band. After a relatively short time, the excited electron will fall back to an available vacancy at the valence band, removing these two charge carriers from the bands, in a process called *recombination.* The time at which the charge carrier is excited on average is called *charge carrier lifetime* or just *lifetime*.

This excitation and recombination process differs for the direct and indirect band gap materials. In direct band gap material, simple excitation of the charge carrier is sufficient to lift the electron from the valence band to the conduction band. With an indirect band gap, a change in the electron momentum is also required together with the excitation. This yields a difference in probabilities in charge carriers to excite and recombine which affects the electronic, optical, and optoelectronic properties of the materials. For example, direct band gap materials have on average higher photon absorption probabilities, which is preferred with thin film solar cells. Also, the photon emitting probability is higher with direct band gap materials, which is beneficial with light-emitting applications such

as lasers and LEDs. Indirect band gap materials on the other hand exhibit on average increased charge carrier lifetimes. This better electrical property is beneficial with a variety of electronic components such as microprocessors.

Electrons are fermions and thus their energy distribution is described with Fermi-Dirac statistics, where the probability of occupancy at available states is written as

$$f(E) = \frac{1}{1 + e^{\frac{E-E_F}{kT}}},$$
(2)

where E is the electron energy, T is temperature, k the Boltzmann's constant, and E_F Fermi level energy. This energy is the energy where the probability of occupied states is equal to ½. A plot of the Fermi-Dirac distribution function, with varied temperatures is seen in Figure 3. At 0 K the function acts as a step function. This describes the earlier situation, where the valence band has all available states filled with electrons and the conduction band is empty of electrons. As the temperature is increased the step-like function is stretched through the E-axis with filling energy states at the conduction band and leaving empty states at the valence band. This in effect describes the thermal excitation of electrons from the valence band to the conduction band due to thermal energy.
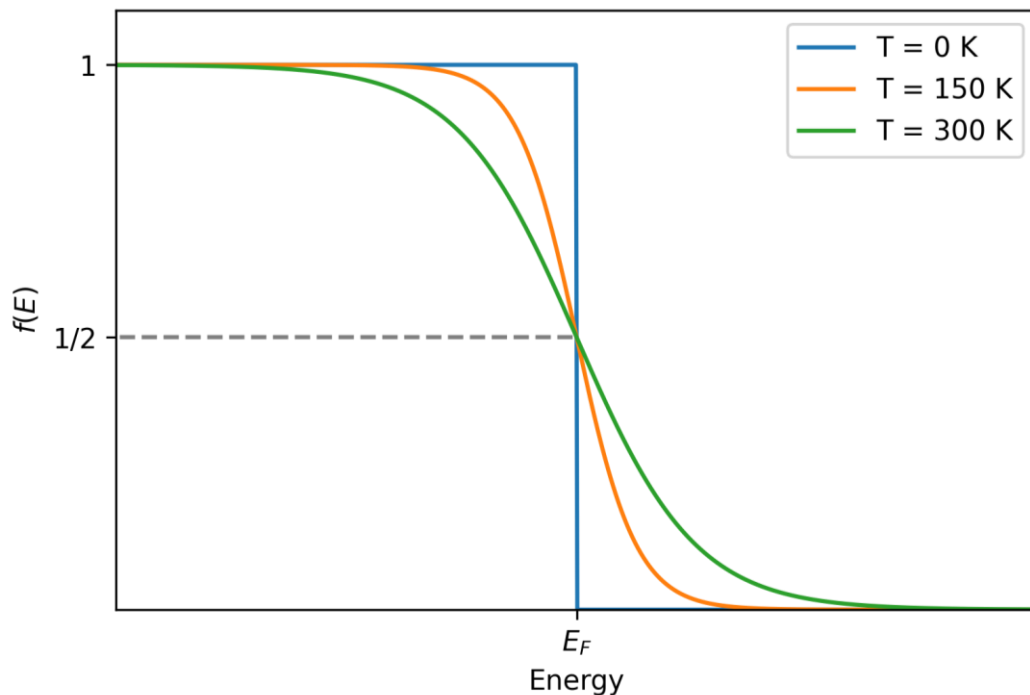

Figure 3. Fermi-Dirac distribution with different temperatures.

A common way to modify the pure *intrinsic* semiconductor lattice is to introduce atoms of another group from which the lattice is formed. This manipulation of the material is called *doping*. By replacing group III atoms with group II atoms, an electron vacancy

(hole) is introduced to the lattice, since group II has one less electron than the replaced atom. This is called p-type doping since we are adding positively charged carriers to the semiconductor and the dopant atoms are referred to as *acceptors*. Name acceptor comes from the fact that the atom "accepts" one electron from the valence band to its spare energy state. (Streetman & Banerjee, 2015)

Similar doping can be done for group V atoms by replacing it with group VI atoms, which introduces extra electrons to the lattice. This is called n-type doping and the dopants are called *donors* since the atom "donates" one electron to the conduction band. Extra charge carriers are loosely bound for their donor or acceptor parent atoms in 0 K, but relatively small energy is sufficient to excite them to the energy bands where they can act as free charge carriers. In most cases, the doped carrier consecration is much higher than the intrinsic carrier concentration resulting from the thermal excitation of electrons. In n-type semiconductors, electrons are referred to as *majority carriers* and holes are referred to as *minority carriers*. This goes vice versa in p-type semiconductors.

When extra charge carriers are introduced to either energy band, the electron energy distribution is changed. Thus, doping affects the Fermi-Dirac distribution, changing the Fermi energy. With the p-type semiconductor, the number of electron vacancies increases, decreasing the probability of finding electrons in the valence band. The Fermi-Dirac distributions, E_F, moves closer to the E_V, when the "tail" of the distribution expands further below the E_V. The same happens with n-type doping where E_F moves closer to the E_C. Changes for the position of the E_F is visualized in Figure 4. This deviation from the bandgap center can be calculated with the following equation for n-type material

$$E_F - E_i = kTln\frac{N_d}{n_i} \tag{3}$$

and for p-type material

$$E_i - E_F = kTln\frac{N_a}{n_i} \tag{4}$$

where E_i is the center energy of the bandgap, n_i is the intrinsic carrier concentration, and N_d and N_a are the doping concentrations for donors and acceptors respectively. (Streetman & Banerjee, 2015)
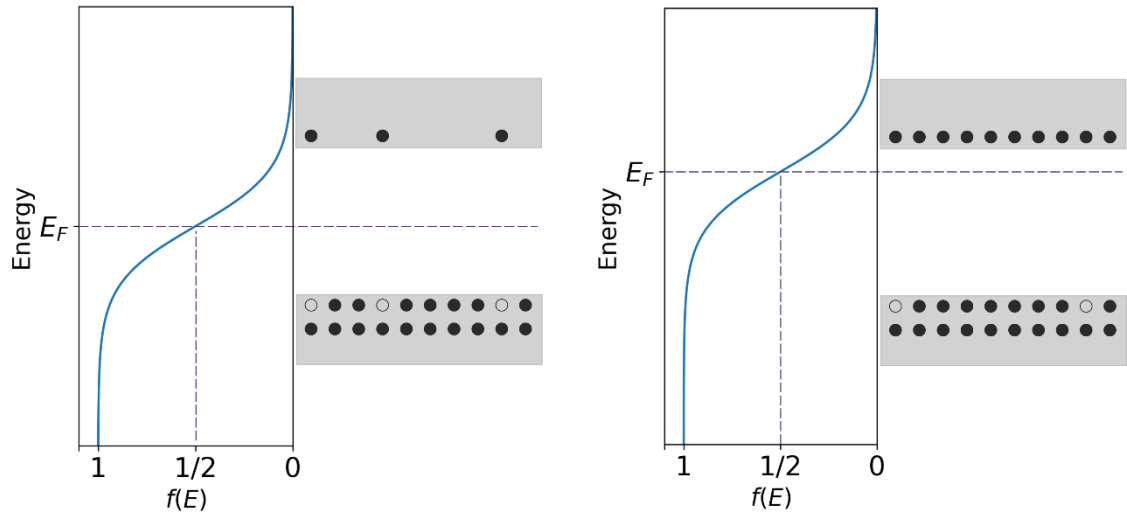
Figure 4. *Effect of n-type doping for the position of the Fermi-Dirac distribution.*

2.2 P–n junction

After learning the basics of semiconductors, we can move to the formation of one of their most famous practical applications of semiconductors, a p–n junctions. This junction is formed between materially connected p-type and n-type semiconductors. A useful thought experiment can be made of the formation of the p–n junction, where p- and n-sides are snapped together, and physical phenomena are "observed" through theory. As the p- and n-type semiconductors are connected, the n-side has more electrons and fewer holes than the p-side and vice versa. Diffusion starts to take place between excess holes and electrons towards the opposite sides. While holes are diffusing from the p-side to the n-side, the complement charges of static acceptor ions are left behind. The same happens for the electrons and their donor atoms. This charge imbalance creates an opposite electric field to the diffusion, which creates an opposite drift current. The electric field increases until the diffusion and drift currents cancel each other out and there is no net current flow inside the p–n junction.

The formation of band diagrams for the p–n junction is seen in Figure 5. In steady-state condition, where no external voltage is applied to the structure, the Fermi level must be constant throughout the structure. With this knowledge, one can connect the Fermi energies of the p- and n-sides and draw the created electric field between the E_V and E_C. This potential of the electric field, referred to as *bias voltage*, can be derived from equations (2), (3), and (4) to a formulation of

$$V_0 = \frac{kT}{q} \ln \frac{N_a N_d}{n_i^2},$$

(5)

where q is the elementary charge. This bias voltage is of high relevance regarding the current–voltage characteristics of the p–n junction-based device.
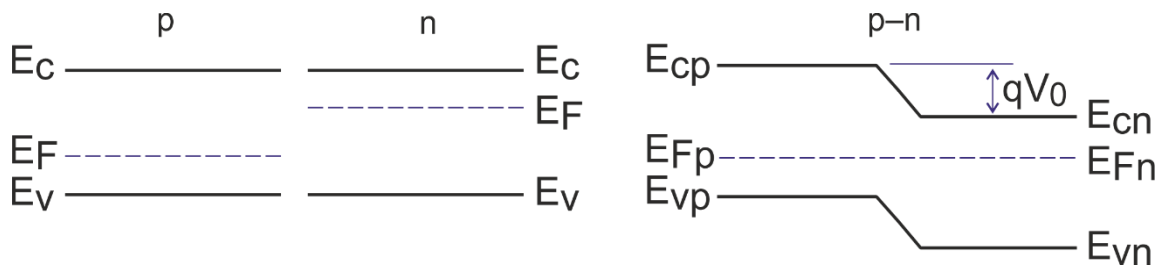

Figure 5. Formation of the energy bands in p–n junction.

An interesting thing happens when voltage is applied to the p–n junction. Rather than creating an electric field across the device, the applied voltage affects the bias voltage of the junction deviating from its nominal value of V_0. When we have positive voltage, defined as having positive bias at the p-side and negative at the n-side, this new junction potential is decreased by the amount of applied voltage. Now we have a weaker barrier to resist the diffusion of charge carriers in the junction, resulting net current flow of holes and electrons from the p to the n-side of the junction and across the device. This diffusion probability increases by the factor of the exponential function of voltage: $\exp(qV/kT)$.

In the negative voltage case, the junction potential is the sum of applied voltage and bias voltage. A small *reverse current* is generated originating from thermally excited EHPs swept across the electric field of the junction. An increase in reverse current saturates relatively fast since the strength of the electric field has little effect on the carrier probability of getting trapped in the influence of the field.

With these effects, we get current–voltage characteristics for the p–n junction

$$I = I_0(e^{qV/kT} - 1), \tag{6}$$

where I_0 is the thermally generated reverse voltage current and V is the applied voltage. As we can predict from equation (6), with the forward bias, our p–n junctions current increases exponentially and at the negative bias current is limited to a small current flow. This device is called a *diode* in electronics and it is an essential component for the electronics industry.

2.3   Photovoltaic cell

One unique feature of semiconductor energy bands is their ability to absorb photons and their associated energy via the excitation of EHPs. This behavior, analogous to an electron excitation at atom orbitals, raises an electron from the valence band to the

conduction band. Excitation is highly probable if the photon energy E_f is equal to or higher than the semiconductor band gap energy E_g. If the created minority carrier is swept to the other side of the junction, it is collected and can be used in an external circuit. In the case of photon energy being higher than the bandgap energy, is the energy difference of $E_f - E_g$ lost in *thermalization losses*, as the carrier gives its energy as heat while bouncing around the lattice. Photons with energy below the bandgap, can't create EHPs in the semiconductor and thus are mainly lost in *transmission loss*. Photon absorption is visualized in Figure 6 Photovoltaic cells utilize this semiconductor behavior to convert light into electricity.
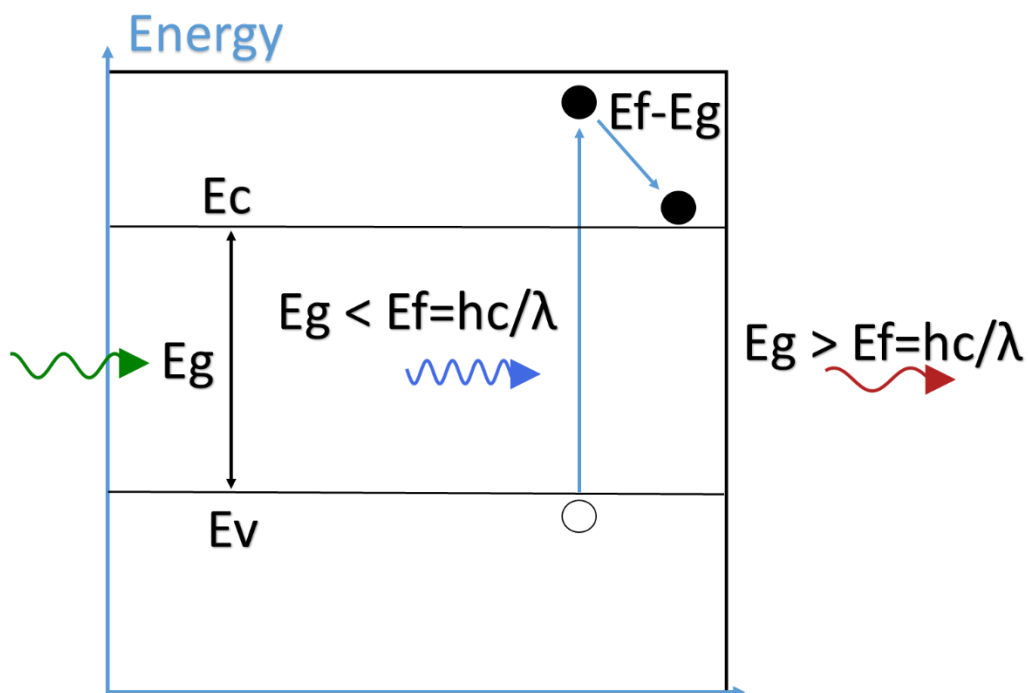

Figure 6 Absorption process of photons by semiconductor energy bands.

When light is introduced to the PV cell, a photogenerated current I_{ph} is added to the p–n junction's current–voltage characteristics of equation (6) and we get

$$I = I_0(e^{qV/kT} - 1) - I_{ph}. \tag{7}$$

A plot of the current–voltage (*I*–*V*) characteristics is shown in Figure 7. From the plot, we can see, that in the 4th quadrant of the current–voltage plot, the PV cell has negative current and positive voltage. From Ohm's law $P = UI$ we get, that the power of the cell is negative i.e., it is producing power to the external circuit. The figure has also some relevant figures of merit highlighted on it: open circuit ($I = 0$) voltage (V_{oc}), short circuit ($V = 0$) current (I_{sc}) and maximum power point voltage (V_{mpp}) and maximum power point

current (I_{mpp}). Maximum power point is the maximum value of power the cell can generate i.e., its optimal load. From equation (7) we get that I_{sc} is equal to I_{ph} and, thus they are often used interchangeably. Maximum power P_{mpp} is the product of the V_{mpp} and I_{mpp}. Another relevant measure of the PV cell I–V curve is the fill factor (FF). It can be described as the squareness of the curve, and it is the area covered by the maximum power point voltage and current divided by the area limited by I_{sc} and V_{oc}. FF can be calculated with a formula

$$FF = \frac{I_{mpp}V_{mpp}}{I_{sc}V_{oc}} = \frac{P_{mpp}}{I_{sc}V_{oc}}. \tag{8}$$

From this equation, we also get a nice representation of the maximum power of the PV cell

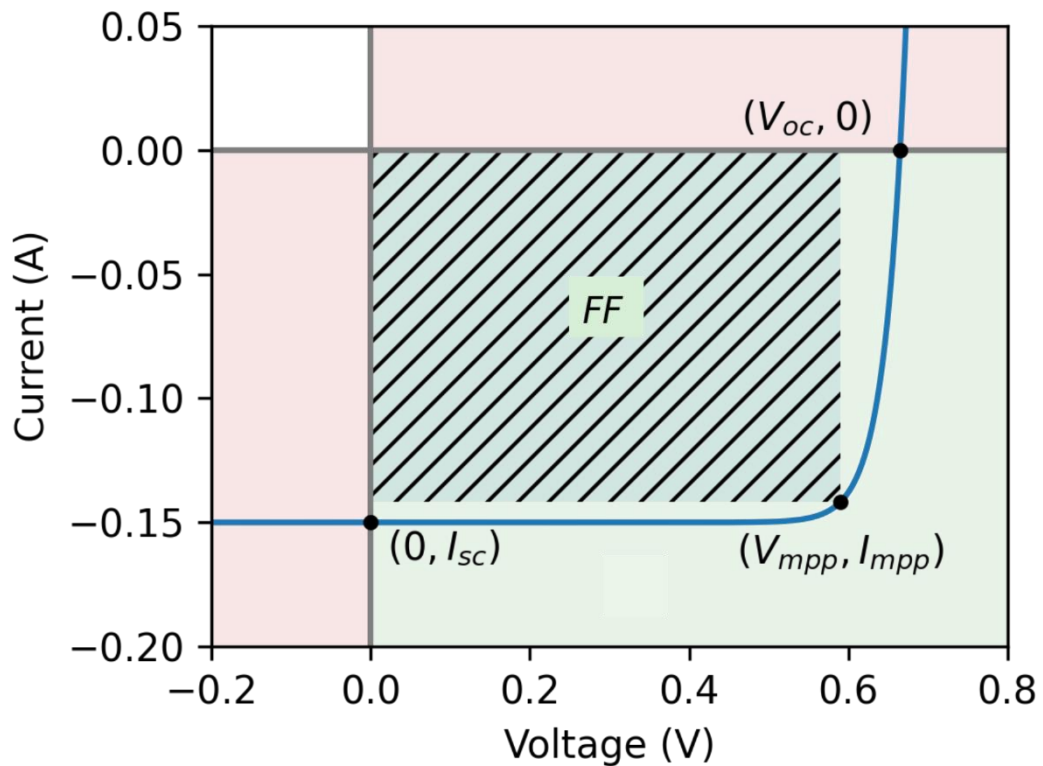$$P_{mpp} = I_{sc}V_{oc}FF. \tag{9}$$

Figure 7. *Current–voltage characteristics of a PV cell.*

From equation (9) we see that by increasing all of the key parameters I_{sc}, V_{oc}, and FF one can increase the maximum power of the device. Value of I_{sc} is influenced by the optical properties of the cell. Simply put: how much light is absorbed. V_{oc} is more measure of the material and junction quality. FF has multiple relations, but it is affected by

material quality, device resistivity and possible shunt currents induced by material defects.

The solar cell is the most known photovoltaic device. It is a PV cell optimized to convert broad-band solar radiation to electricity as efficiently as possible. One interesting challenge arises when we see the energy distribution of the solar radiation in Figure 8. The solar spectrum is distributed in wide bandwidth of wavelengths. By using one semiconductor material as the absorber, we lose a lot of energy in both thermalization and transmission losses.

One way to overcome this spectral mismatch is to split the spectrum for different solar cells with different bandgaps. This can be realized by splitting the light based on wavelength to separate solar cells or by stacking solar cells with different bandgaps on top of each other. By adding cells with varied bandgaps, the energy difference between high-energy photons and bandgaps decreases as well as the number of lost photons in transmission loss. Figure 9 has the solar cell theoretical efficiencies plotted as a function of the number of junctions based on calculations by (Brown & Green, 2002).
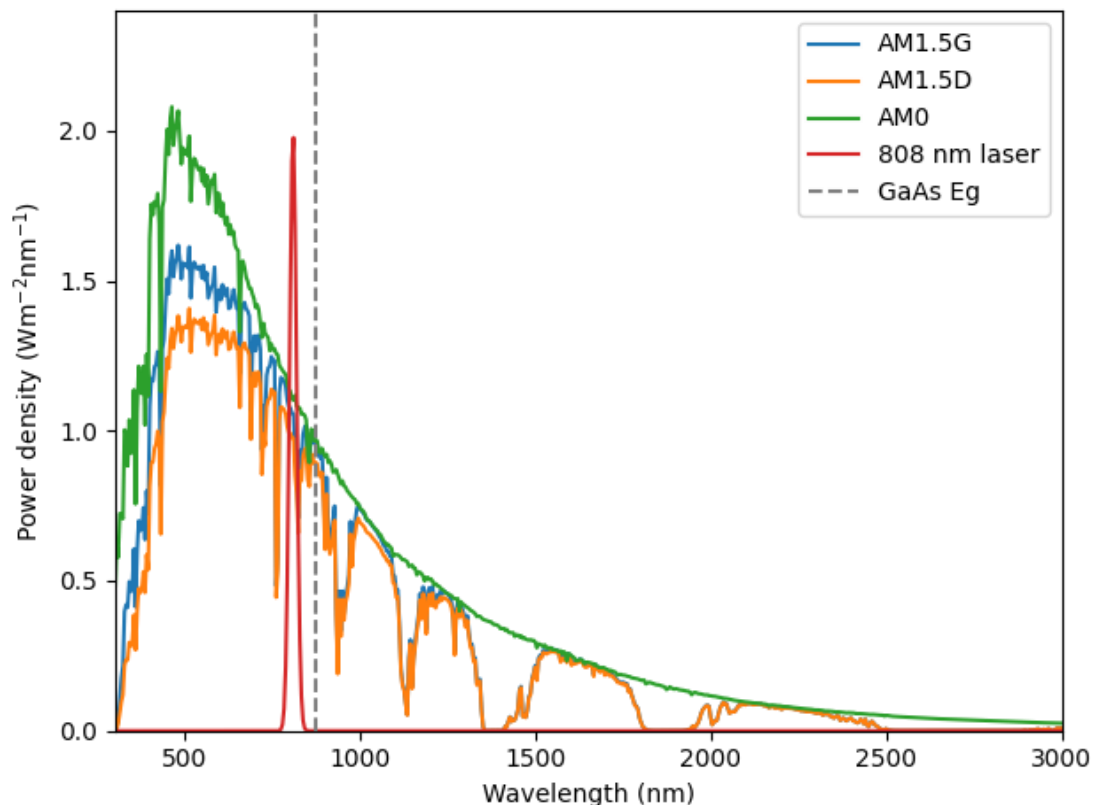

Figure 8. Different solar spectrums for space (AM0) and for terrestrial cases (AM1.5 G and D)(ASTM International, 2019, 2020), example spectrum for a 808 nm laser diode and a band gap equivalent wavelength of GaAs.

Another highly interesting PV cell variant is the photovoltaic converter. PV converters are optimized for narrow-band light sources like lasers or LEDs and are used in power-by-light applications. In PbL, energy is transferred via light instead of electricity, and was firstly demonstrated by (DeLoach et al., 1978). This is realized by converting electricity to light via a high-power laser or LED. Light is then transferred via optical fiber or free space to a PV converter, which converts the energy back to electricity where it can power wanted electronic devices. PbL technology is used in applications requiring e.g., power delivery with galvanic isolation (De Nazaré & Werneck, 2012). One additional interesting advantage of the PbL technology is the ability to use an existing optical fiber infrastructure to power up some newly deployed devices like 5g C-RAN station (Lopez-Cardona et al., 2021).
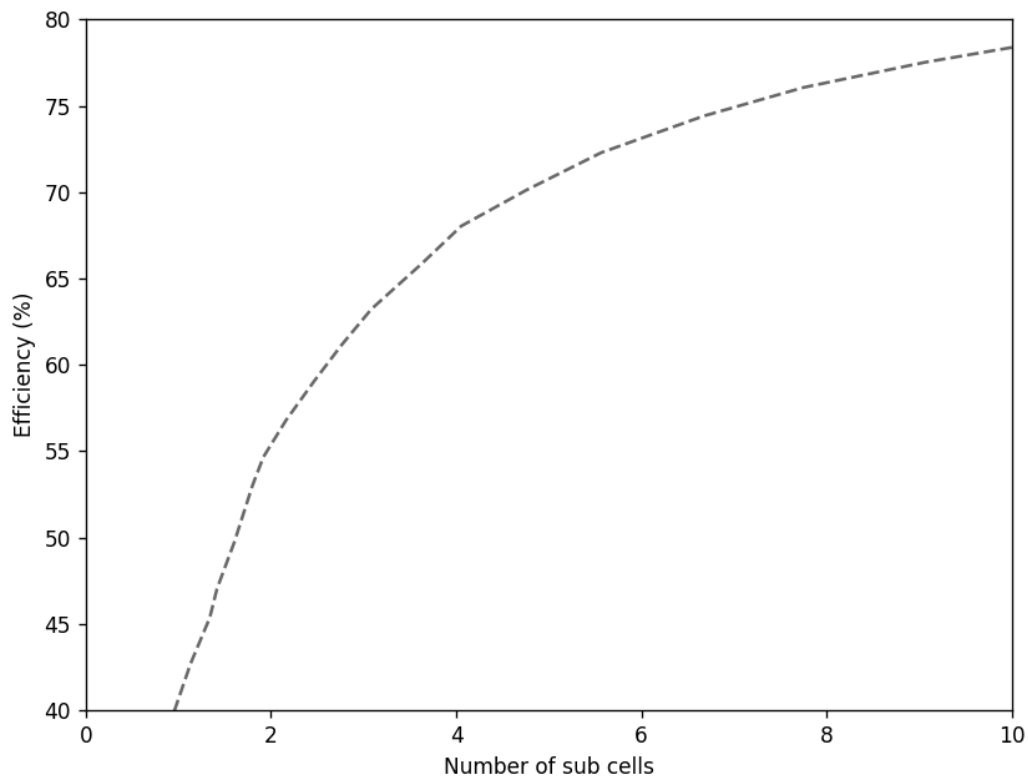

Figure 9. *Theoretical solar cell efficiency as a function of optimally chosen subcells. Results from (Brown & Green, 2002).*

Compared to the solar spectrum, the output spectra of a laser are considerably narrower. Whereas solar radiation has over 2000 nm wide bandwidth, laser diodes have in the range of 10 nm or less. With this optimal spectral distribution, one can fabricate a PV material with bandgap energy slightly higher than the photon energy of the peak emission. This results in virtually no absorption losses and at the same time thermalization

losses are kept to a minimum. For example, for GaAs with a bandgap of 1.424 eV and for an 830 nm light with a photon energy of 1.494 eV, the thermalization loss is approximately only 5%. Compared to the case of a single junction GaAs solar cell under the AM1.5G irradiation, where roughly 21 % of the photon energy is lost in the thermalization loss and another 34 % to the transmission loss when other losses are not being accounted for.

2.4   Resistive losses and front contact grid

Resistive losses play a key part in components, where a high enough current is flowing. This is often the case with photovoltaics, and especially true for PV converters. From Ohm's law, resistive loss (i.e., generated heat power) of an electrical component is

$$P = I^2 R, \tag{10}$$

where R is the component resistance. We can see that there are two ways of decreasing the generated loss: by decreasing the current going through the device and by lowering its resistance. Decreasing the current and ramping up the device's operating voltage is plausible to an extent, but it requires smart design consideration (Fafard & Masson, 2021), which can only lead so far. Thus, we are left with lowering the resistance of the PV device, often denoted as *series resistance*. With series resistance, we see a clear room for improvements since semiconductors have relatively high resistivities at room temperature. On the other hand, metals are known to have high conductivities, and thus directing the generated photocurrent through metal lines can reduce the resistivity and resistive losses of the cell considerably.

Front contact grid metallization has been an established solution for minimizing the resistive losses due to the lateral current flow from the active area to connection terminals of the cell, called busbars. However, addition of this metallization introduces a new loss mechanism for the cell, shading. Due to the metals not being transparent in the solar spectrum (Bartek et al., 1999; Johnson & Christy, 1972), all light hitting the metallization pattern is mostly reflected back and not absorbed by the PV cell. A sketch of the front contact grid and the associated shading loss is shown in Figure 10.

This tradeoff in adding conductive but nontransparent metal on top of the cell creates an optimization problem: what is the right pattern and amount of metal to maximize the light going in the cell and minimize the resistance of the device?
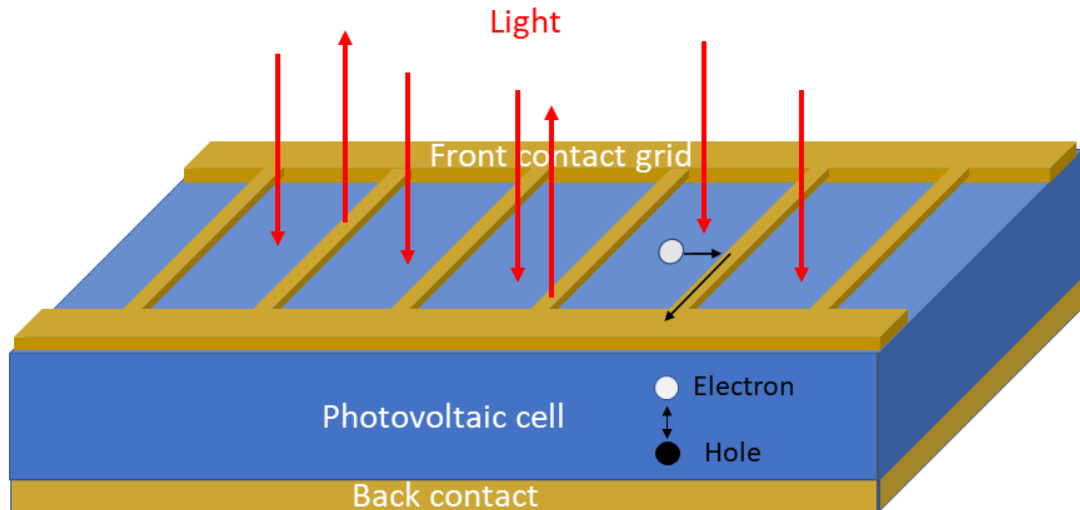
Figure 10 *Sketch of a front contact grid in aiding the current transport in PV cell and the resulting shading loss from the metal coating* (Nikander et al., 2021)*. Use under CC 4.0.*

Various front contact grid patterns are used, like traditional two-busbar finger grid (Hong et al., 2014a), inverted square (Huo & Rey-Stolle, 2017), circular pattern (Oliva et al., 2008) and even some complex computer-optimized designs (Gupta et al., 2016). All these designs have their own advantages and disadvantages. While the two-busbar finger grid is simple to design and manufacture and performs well in most cases, the inverted square excels in concentrator applications and circular pattern in power over fiber illumination. Examples of two-busbar, inverted square, and circular front contact grid designs are shown in Figure 11.
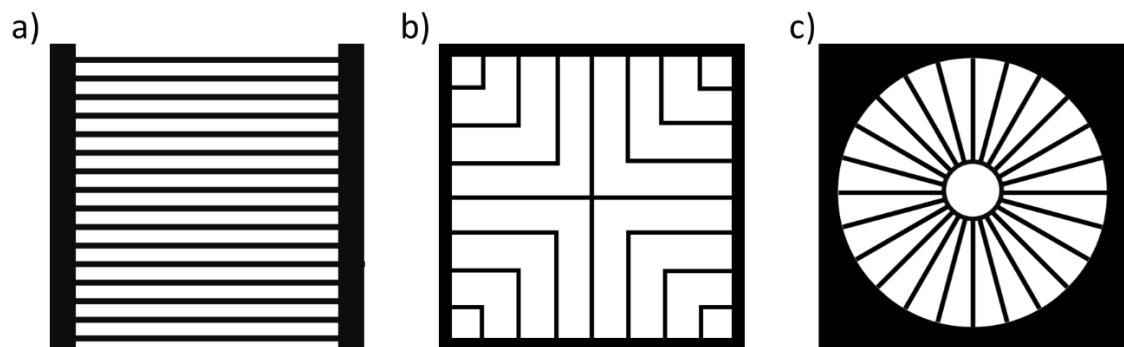

Figure 11 *Simplified sketches of finger grid patterns for a) a two-busbar, b) an inverted square, and c) a circular design.*

Regardless of the pattern design, it is beneficial to do as narrow and as tall fingers as possible to minimize the shading with a given added metal. A common width of the fingers is in the range of 5 µm (Hong et al., 2014b; Ward et al., 2015). As the width and height of the fingers are rather limited to the fabrication processes, the main design consideration for the finger patterns is the amount of the fingers fabricated on the cell i.e.,

their *spacing*. Spacing is the distance between two fingers. In two-busbar finger grid and inverted square grid it can be expressed in length, which typically is in the range of 100 µm at high power applications. For the circular pattern, a pitch angle of the fingers would be a better measure of spacing. Some other design considerations in front contact metallization are choosing the metal alloy used in the grid (Ward et al., 2015) and ensuring good ohmic contact at the metal-semiconductor junction (Vinod, 2008). These problems are out of the scope of this work and will not be addressed.

Since the PV cell is a diode, the device resistance cannot be determined by just measuring the voltage loss across the device by given a current. One way to analyze the series resistance of a PV cell is to study the device FF values. Although device resistance is not the only factor affecting the FF, it has profound effects, especially, when high resistive losses are present. Figure 12 shows the effect of series resistance on PV cells current–voltage behaviour.
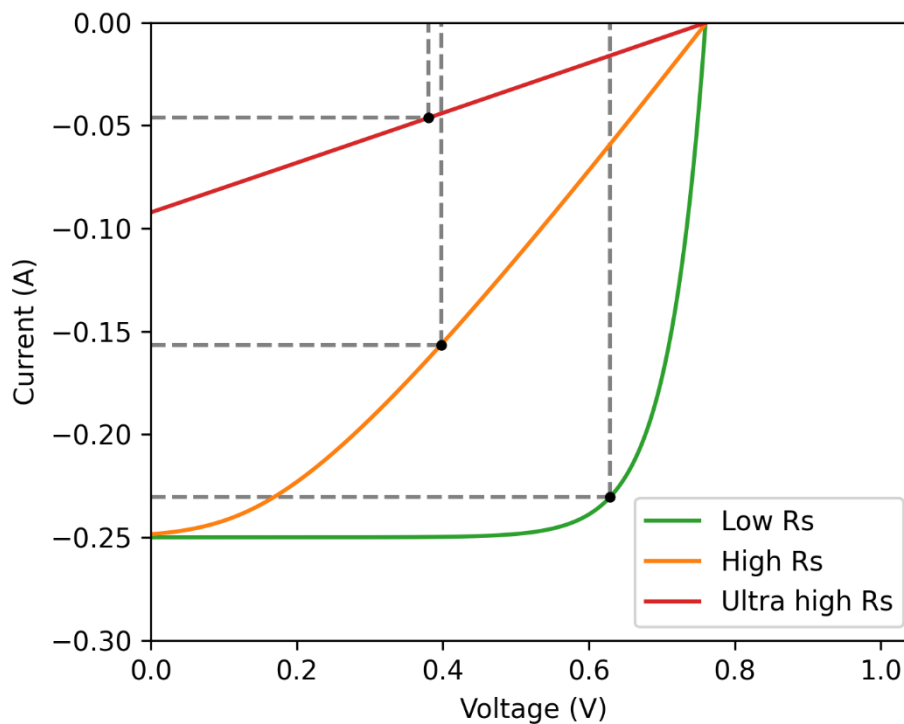

Figure 12 *Current–voltage behaviour of PV devices with various levels of series resistance (Rs), and effect on the device the FF and I_{sc}.*

2.5   Temperature effects on the photovoltaic cell

One often overlooked aspect of the PV cell performance is the operational temperature of the device. The effect of increased temperature is profound for any photovoltaic device. Temperatures effect on the material band gap can be described by Varshni (1967) relation

$$E_g(T) = E_{g,0} - \frac{\alpha T^2}{T + \beta},$$
(11)

where $E_{g,0}$ is the band gap energy at 0 K, T is temperature and α and β are material dependent coefficients. This change in band gap energy has ramifying effects on both optical and electrical properties of the optoelectronic device. With increased temperature the absorption coefficient of the material increases. For single junction designs this does not matter, it can even slightly increase the photon generation since some photons lost in transmission loss are now absorbed by the narrower band gap. But with multi-junction designs, this change in the current a generation can lead to generation miss match between the subcell, which can have a detrimental effect on the cells photo generated current (Reichmuth et al., 2017).

Another factor having a major effect on cell performance is the reduction of V_{oc} with the increased temperature. V_{oc} relation with temperature can be expressed by following

$$\frac{dV_{oc}}{dT} = \frac{\frac{1}{q} E_{g,0} - V_{oc} + \xi \frac{kT}{q}}{T},$$
(12)

where ξ is a recombination dependent coefficient. Major micro-level effects on the decrease of V_{oc} are the increased intrinsic carrier concentration which is induced by narrower a band gap and "wider" fermi distribution, such that more thermally excited electrons can jump from the valence band to the conduction band. Increased intrinsic carrier concentration decreases the dark saturation current which leads to smaller V_{oc} value and smaller maximum power.

3. SIMULATION TOOLS

Throughout over 60 years of photovoltaics academic and industrial history, various tools have been developed and adopted from other fields to design, simulate, optimize, and analyze PV devices. Most of these tools are surprisingly intuitive and they wrap neatly the complex physics working in the background into easy-to-understand models. In this work, rigorous and efficient simulation tools have been selected and utilized for a novel combined simulation tool, the Hybrid quasi-3D model. Selected tools, except for a double diode model are implemented from Solcore, a Python-based library for modelling solar cells and semiconductor materials (Alonso-Álvarez et al., 2018). Here we go through all the simulation models on which the Hybrid quasi-3D model is built and, in the end, the tool itself is described.

3.1   Transfer matrix method

The transfer matrix method is an efficient tool for modelling 1D thin film structures such as anti-reflection coatings (Benamira & Pattanaik, 2020) and photovoltaic cells (Shabat et al., 2018). The following formalism is derived from (Yeh, 2005). The method relies in the wave formalism of light where an oscillating electric field is written as

$$E = E(x)e^{i(\omega t - \beta)}, \tag{13}$$

where ω is the angular frequency, β is phase shift and t is time. For the multilayer case seen in Figure 13, the structure consists of layers with varying refractive index and thickness which are defined as

$$n(x) \begin{cases} n_0, & x < x_0, \\ n_1, & x_0 < x_1, \\ n_2, & x_1 < x_2, \\ \vdots \\ n_N, & x_{N-1} < x_N, \\ n_s, & x_N < x, \end{cases} \tag{14}$$

and $E(x)$ is defined as

$$E(x) = \begin{cases} A_0 e^{-ik_{0x}(x-x_0)} + B_0 e^{ik_{0x}(x-x_0)}, & x < x_0, \\ A_l e^{-ik_{lx}(x-x_l)} + B_l e^{ik_{lx}(x-x_l)}, & x_{l-1} < x < x_l, \\ A'_s e^{-ik_{sx}(x-x_N)} + B'_s e^{ik_{sx}(x-x_N)}, & x_N < x, \end{cases} \tag{15}$$

where k_{lx} is

$$k_{lx} = \left[\left(n_l \frac{\omega}{c}\right)^2 - \beta^2\right]^{1/2}, \qquad l = 0,1,2,\dots,N,s. \tag{16}$$

The A-field represents the light propagating to the positive x-direction in different parts of the multilayer structure and the B-field represents the negative direction.
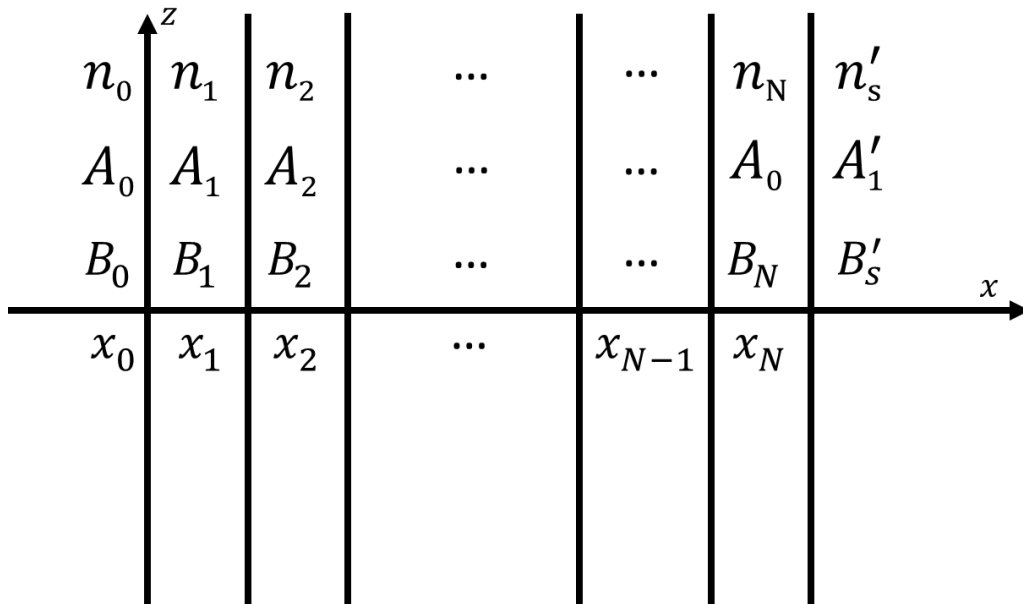

Figure 13. *sketch of general formalism for a multilayer structure.*

Interaction of light fields at a given interface can be represented with a formulation

$$\begin{pmatrix} A_l \\ B_l \end{pmatrix} = D_l^{-1} D_{l+1} \begin{pmatrix} A_{l+1} \\ B_{l+1} \end{pmatrix}, \tag{17}$$

where the D matrix is defined for the s-polarized light as

$$D_l = \begin{pmatrix} 1 & 1 \\ n_l \cos(\theta_l) & -n_l \cos(\theta_l) \end{pmatrix}, \tag{18}$$

and for the p-polarized as

$$D_l = \begin{pmatrix} \cos(\theta_l) & \cos(\theta_l) \\ n_l & -n_l \end{pmatrix}, \tag{19}$$

where θ_l is the angle of incidence for the light, which is 0 in most photovoltaics cases, simplifying the D matrix

$$D_l = \begin{pmatrix} 1 & 1 \\ n_l & -n_l \end{pmatrix}, \tag{20}$$

for both polarizations. Propagation and possible gain and absorption in the given layer l is represented with a matrix

$$P_l = \begin{pmatrix} e^{ik_{lx}(x_l - x_{l-1})} & 0 \\ 0 & e^{-ik_{lx}(x_l - x_{l-1})} \end{pmatrix}. \tag{21}$$

Effect of the thin film structure for electric fields A_0, B_0, A_s' and B_s' outside the thin film can be formulated with P_l and D_l matrices to a following form

$$\begin{pmatrix} A_0 \\ B_0 \end{pmatrix} = D_0^{-1} \left[\prod_{l=1}^{N} D_l P_l D_l^{-1} \right] D_s \begin{pmatrix} A_s' \\ B_s' \end{pmatrix}, \tag{22}$$

where the matrix product of the D and P matrices is denoted with

$$D_0^{-1} \left[\prod_{l=1}^{N} D_l P_l D_l^{-1} \right] D_s = \begin{pmatrix} M_{11} & M_{12} \\ M_{21} & M_{22} \end{pmatrix}, \tag{23}$$

yielding

$$\begin{pmatrix} A_0 \\ B_0 \end{pmatrix} = \begin{pmatrix} M_{11} & M_{12} \\ M_{21} & M_{22} \end{pmatrix} \begin{pmatrix} A_s' \\ B_s' \end{pmatrix}. \tag{24}$$

The reflection coefficient for incident light propagating in the positive x-direction ($B_s' = 0$) is defined as

$$r = \left(\frac{B_0}{A_0} \right), \tag{25}$$

and a transmission coefficient is defined as

$$t = \left(\frac{A_s'}{A_0} \right). \tag{26}$$

From equation (24) we get for r

$$r = \frac{M_{21}}{M_{11}}, \tag{27}$$

and for

$$t = \frac{1}{M_{11}}. \tag{28}$$

For the reflected power, the coefficient for electric field needs to be squared. Thus, we get for the thin film reflectance

$$R = |r|^2 = \left| \frac{M_{21}}{M_{11}} \right|^2, \tag{29}$$

and for the transmittance

$$T = \frac{n_s \cos (\theta_s)}{n_0 \cos (\theta_0)} |t|^2 = \frac{n_s \cos (\theta_s)}{n_0 \cos (\theta_0)} \left| \frac{1}{M_{11}} \right|^2. \tag{30}$$

3.2 Poisson-drift-diffusion model

The Poisson-drift-diffusion (PDD) model is one of the more detailed simulation tools for simulating the current–voltage characteristics of PV cells. It models the drift and diffusion currents going through a 1D energy band structuring of the junction. The total current density inside the PV cell is the sum of a hole and an electron currents

$$J = J_p + J_n, \tag{31}$$

which are J_p and J_n respectively. Respective currents are further a sum of the drift and diffusion currents. For electrons are they are defined as

$$J_n = J_n^{diff} + J_n^{drift} \tag{32}$$

$$J_n^{diff} = \mu_n k_b T \frac{dn}{dx} \tag{33}$$

$$J_n^{drift} = q\mu_n F, \tag{34}$$

where F is the electric field and μ_n is the electron mobility. For holes the currents are

$$J_p = J_p^{diff} + J_p^{drift} \tag{35}$$

$$J_p^{diff} = -\mu_p k_b T \frac{dp}{dx} \tag{36}$$

$$J_p^{drift} = q\mu_p F, \tag{37}$$

where μ_p is the hole mobility. (Luque & Hegedus, 2010)

Under a steady state condition i.e., without applied external voltage, there is no net flow of charge carriers, resulting a balance of a generation rate, a recombination rate, and carrier currents:

$$\frac{dJ_n}{dx} + qG - qR_e = 0 \tag{38}$$

$$-\frac{dJ_p}{dx} + qG - qR_e = 0, \tag{39}$$

where G in the photo generated carrier generation rate and R_e is the recombination rate of the excited carriers. Combining equations (32) and (40) we get

$$q\mu_n \left(\frac{k_b T}{q} \frac{d^2 n}{dx^2} + F \frac{dn}{dx} + n \frac{dF}{dx} \right) + qG - qR_e = 0. \tag{40}$$

And from equation (35) and (39) we get

$$q\mu_p \left(\frac{k_b T}{q} \frac{d^2 p}{dx^2} - F \frac{dp}{dx} - p \frac{dF}{dx} \right) + qG - qR_e = 0. \tag{41}$$

When combined with the Poisson's equation describing the junction potential with the dopant ions:

$$\frac{d}{dx} \left(\epsilon \frac{d\phi}{dx} \right) + q(p - n + N_d - N_a) = 0 \tag{42}$$

we can describe the system and solve problems such as carrier concentrations, quasi fermi levels and most importantly the current–voltage characteristics of the given structure.

3.3 Double diode model fitting

The double diode model (DDM) is another 1D description of PV devices. It tries to create an accurate, yet efficient and simple circuit equivalent model of the physical processes inside a PV cell. With various versions of the diode model descriptions, DDM strikes a good balance with the above criteria. Model is a circuit reconstruction of the PV cell, consisting of two diodes in parallel with a current source, a shunt resistor and one series resistor. The circuit diagram of the DDM can be seen in Figure 14. The current source models the photogenerated current, the series resistor all the resistive losses inside the cell and the shunt resistor models shunt currents induced by unwanted defects. The two diodes model the recombination currents inside the junction. The first diode models the recombination outside the junction's electric field. This region is called a *quasi-neutral region*. The second diode on the other hand describes recombination currents at the junction electric field, called the *space charge region*.
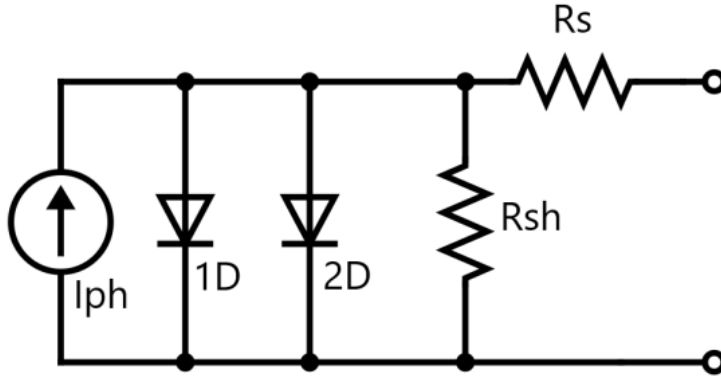
Figure 14. *Circuit equivalent model of the DDM* (Nikander, 2020).

The current going through the circuit can be written as

$$I = I_{ph} + I_{01}e^{\frac{V+IR_s}{V_T}} + I_{02}e^{\frac{V+IR_s}{2V_T}} - \frac{V+IR_s}{R_{sh}}, \tag{43}$$

where I_{01} is the reverse current of 1D, I_{02} is the reverse current of 2D, R_s is the resistance of the series connected resistor and R_{sh} is the resistance of the shunt resistor. (Luque & Hegedus, 2010)

Equation (43) is a transcendental equation, meaning that it can't be represented with a finite number of algebraic operations (Hazewinkel, 1995). This comes from the addition of series resistance, which adds current terms to the exponents of the diode equations. One can solve this kind of problem with Lambert W-function (Corless et al., 1996), which solves y from equation

$$ye^y = x \tag{44}$$

$$y = W(x), \tag{45}$$

where $W(x)$ is the Lambert W-function. When applied to equation (43) one can solve the I as follows

$$I = \frac{R_{sh}(I_{ph} + I_{01} + I_{02}) - V}{R_s + R_{sh}} - r\frac{n_1 V_T}{R_s}W(\theta_1) - (1-r)\frac{n_2 V_T}{R_s}W(\theta_2), \tag{46}$$

where

$$\theta_1 = \frac{I_{01}R_s R_{sh}}{rn_1 V_T(R_s + R_{sh})}exp\left[\frac{R_{sh}(R_s I_{ph} + R_s I_{01}/r + V}{n_1 V_T(R_s + R_{sh})}\right] \tag{47}$$

$$\theta_2 = \frac{I_{02}R_s R_{sh}}{(r-1)n_2 V_T(R_s + R_{sh})}exp\left[\frac{R_{sh}(R_s I_{ph} + R_s I_{02}/(1-r) + V}{n_2 V_T(R_s + R_{sh})}\right] \tag{48}$$

$$r = \frac{I_{01}\left[\exp\left(\frac{V + IR_s}{n_1 V_T}\right) - 1\right]}{I_{01}\left[exp\left(\frac{V + IR_s}{n_1 V_T}\right) - 1\right] I_{02}\left[exp\left(\frac{V + IR}{n_2 V_T}\right) - 1\right]}. \tag{49}$$

DDM is a useful model since it gives us a reasonably accurate depiction of the PV cell as an electrical component. It enables incorporating photovoltaics as a part of a circuit simulation, giving PV engineers a powerful tool to develop systems relying on PV components.

DDM equation parameters can be estimated based on the physics of optoelectronics. Skillful engineer or scientist can also extract the parameters from the PV cell by fitting the equation to current–voltage measurement of the PV cell. With adequate fitting, one can deepen the PV analysis from the macro to the micro level with the component parameters.

3.4 Quasi-3D model

All the above-mentioned tools are either restricted to a 1D representation of the PV device or in the case of DDM to macro-level behavior. They work well to an extent when designing and analyzing PV structures, but some problems in PV engineering and science require a 3D representation of the cell. Effects such as lateral current flow and uneven illumination require entering the more demanding field of 3D modelling. With a Quasi-3D model, we can enter this dark side of simulations with relative comfort and intuition while getting the most benefits of the 3D realm.

In the Quasi-3D model, a PV cell is divided into small subcomponents represented by DDM. These sub-components are connected to each other laterally by resistors, which model the lateral resistance of current flow. This lateral resistance of the material is called sheet resistance, which can be calculated for a semiconductor material by equation

$$R_{sheet} = \frac{1}{\mu q N d} \tag{50}$$

where μ is the majority carrier mobility, N is the carrier concentration and d is the given layer thickness. Doping concentration is used often as an approximate for N. The front contact grid is also built on top of this discretization. The shadowing effect under the contacts is taken into account by removing the current source from the sub-cells underneath the metal contacts. Quasi-3D model also allows to model effects of uneven illumination profiles, by scaling the photogenerated current based on the given illumination profile matrix.

After the 3D component matrix is created from the cell representation, it is inserted into a *simulation program with integrated circuit emphasis* (SPICE) solver. This solver then calculates the *I–V* curve and 2D top-view voltage profile for the cell. A voltage profile can be used for detecting the critical limitations in lateral current flow or even in modelling the electroluminescence of the device (Alonso-Álvarez & Ekins-Daukes, 2016). By calculating the *I–V* curve, one can determine performance parameters V_{oc}, I_{sc} and FF, from which one gets the P_{mpp} and efficiency of the device.
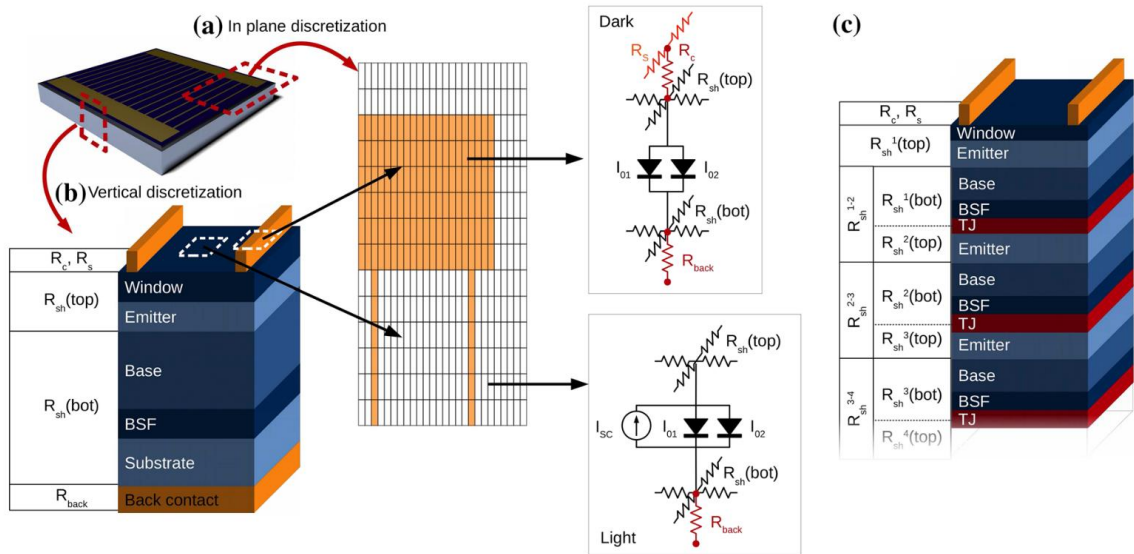

Figure 15. *Sketch of the quasi-3D discretization scheme.* (Alonso-Álvarez et al., 2018). Use under CC 4.0.

3.5   Hybrid Quasi-3D model

We have explored useful simulation tools to describe different parts of photovoltaic performance. All these tools are well established in different optimization problems of photovoltaics and in this work combined model, Hybrid quasi-3D (HQ3D) model is constructed based on all the presented simulation models. The simulation model is developed with Python 3 coding language (Python.org), utilizing Solcore (Alonso-Álvarez et al., 2018), a multi-scale library for modelling photovoltaics and semiconductor materials. All the implemented photovoltaic simulation models used in the HQ3D are taken from Solcore, apart from DDM, which has been implemented in Python by the author based on (Gao et al., 2016).

The simulation starts with the user defining the thin film layer structure and contact grid design parameters and illumination profile. Then Solcore TMM model originally developed by (Byrnes, 2016) is used to model the 1D optics and absorption profile of the layer structure, which is then inserted into the PDD. It solves the *I–V* characteristics of the

layer structure to which DDM is fitted with a fast Nelder-Mead fitting algorithm (Nelder & Mead, 1965). After 1D simulations, the solver moves to initialization of the discretized PV structure for the quasi-3D solver, by creating the device discretization based on the given front contact grid design. The device is split into the smallest possible slices in order to reduce the calculation time of the quasi-3D solver, which increases exponentially with the size of the device. With the double busbar design, the smallest possible symmetry is a slice of one finger, cut in half at the horizontal line of the finger. I.e., by multiplying these sections, one can construct the entire cell. Figure 16 shows the discretization on the double busbar finger grid design. In the case of uneven but circularly symmetrical illumination, subcells constituting one quadrant of the cell are simulated and the current of their I–V curves are added together and factored by four to yield the complete I–V curve of the cell. As for uneven illumination without symmetry, all of the subcells have to be simulated and summed together.
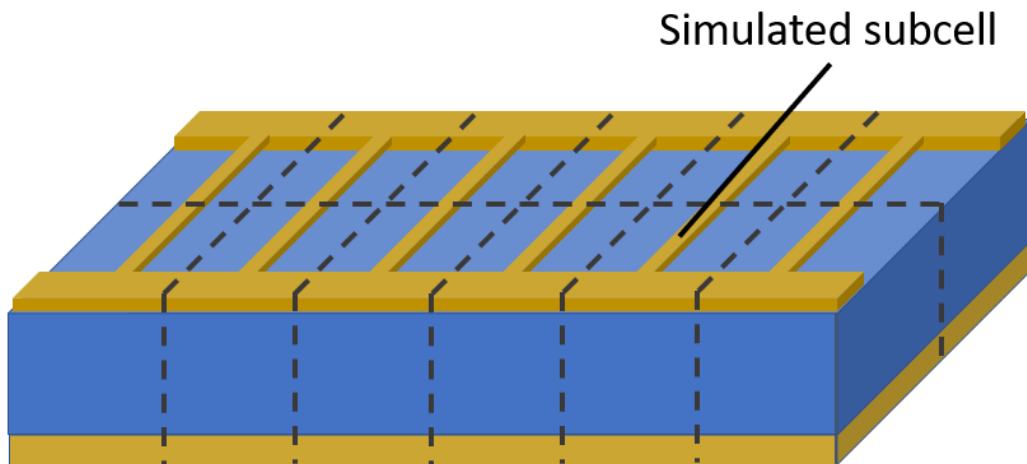

Figure 16 *Discretization of the double busbar finger grid.*

After the discretization, the solver forms a front contact grid and illumination matrices to match the subcells. These matrices and DDM are inserted into the quasi-3D solver, which creates the 3D circuit matrix. This 3D circuit is inserted into SPICE solver *ngspice* (Ngspice), which solves the current–voltage characteristics for the 3D device. From the current–voltage curve we can extract relevant measures: FF, V_{oc}, I_{sc} and P_{mpp} as described in Chapter 2 for further analysis. The flow of the HQ3D simulation is shown in Figure 17.
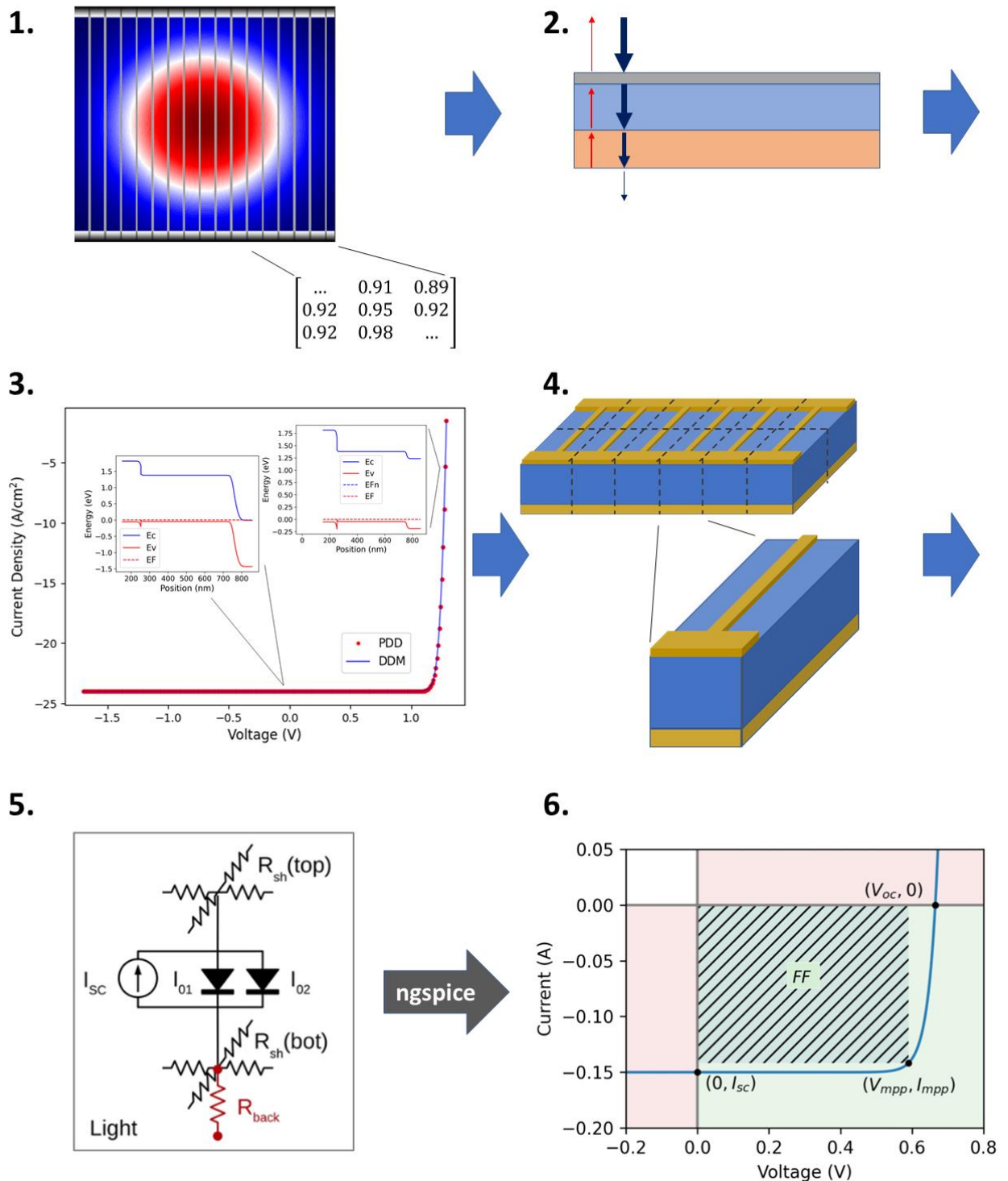
Figure 17 *Flow of the HQ3D simulation model:* **1.** *Grid and illumination matrices are generated* **2.** *TMM is used to calculate the photon absorption,* **3.** *PDD is used to determine the 1D IV curve and DDM is fitted to it,* **4.** *Discretization it determined based on the grid and illumination geometry,* **5.** *Grid and illumination matrices are generated and inserted with the DDM to the Q3D solver which Q3D creates a 3D circuit equivalent matrix (cropped from (Alonso-Álvarez et al., 2018) under CC 4.0.), and* **6.** *ngspice solves the IV curve where parameters such as* FF, V_{oc}, I_{sc}, *and* P_{mmp} *can be extracted.*

4. GRID DESIGN OPTIMIZATION

The Hybrid quasi-3D model is utilized in the optimization of front contact grid metalliza-tion. Two-busbar finger grid design is considered and the spacing of the fingers is opti-mized, for two similar, but inverted single junction PV converter structures under four different illumination profiles and for three operation temperatures. Before the grid opti-mization, PV structures are defined, and the effect of different illumination profiles are simulated and discussed. Optimal beam profiles from this simulation are used in the grid optimization. Lastly, deeper analysis of the cell behavior under varied operation condi-tions is done.

4.1 Simulated structure

In this work, a p–n structure from (Vänttinen et al., 1995) and a similar inverted n–p structure is considered, which are shown in Figure 18. A cell area of 5 mm x 5 mm is chosen. Two-busbar gold front contact finger grid with cross-section of the finger of 4.5 μm^2 is used, to match a realistic case. Discreditation scheme of 500 pixels parallel to and 1667 perpendicular to the fingers is deployed for the whole device. Solcore's default material parameters are used which are from (Vurgaftman et al., 2001) for energy band parameters, (Sotoodeh et al., 2000) for charge carrier mobilities and indices of refraction are form (Software Spectra Inc. 2008). For the conductivity of the front contact grid metal, the conductivity of bulk gold from (Serway & Jewett, 2006) is used. Table 1 has param-eters relevant to the current spreading of the top photovoltaic layer, often referred to as an *emitter*. The current spreading of the emitter layer constitutes for the efficient current transport of the carriers and dictates the need for front metallization. These parameters are the top GaAs layer doping, majority carrier mobility and the resulting sheet re-sistance.

Table 1 *Material parameters and the resulting sheet resistance of the emitter layers (layers on top of the junction).*

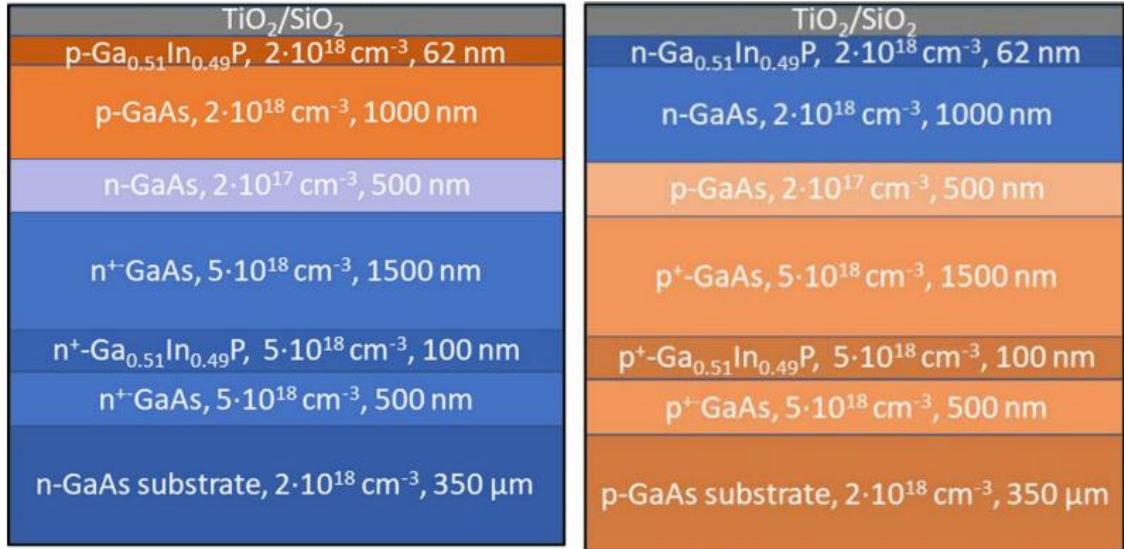|	Doping (cm^{-3})	Mobility (cm^2 / Vs)	Sheet resistance for 1000 nm layer (Ω / sq)
p-GaAs	$2 \cdot 10^{18}$	150	222
n-GaAs	$2 \cdot 10^{18}$	2300	14

Figure 18. *Simulated p–n* (Vänttinen et al., 1995) *structure on the left and n–p structure on the right.* (Nikander et al., 2021). *Use under CC 4.0.*

4.2 Illumination profiles

Common output power distribution from a multimode optical fiber is in a form of super-Gaussian distribution, which can be expressed with function

$$I(r,z) = I_{max} \left(\frac{w_0}{w(z)} \exp \left(- \left(\frac{r}{w(z)} \right)^{2g} \right) \right)^2, \tag{51}$$

where

$$w(z) = w_0 \sqrt{1 + \left(\frac{z}{z_R} \right)^2} \tag{52}$$

and

$$z_R = \frac{\pi w_0^2 n}{\lambda} \tag{53}$$

where I_{max} is the maximum irradiance, $w(z)$ is the beam waist, w_0 is the beam waist at the focus point, n is the refractive index of transfer medium, λ is the wavelength of the propagating light, z is the distance from the focus point and g is the Gaussian order (Shealy & Hoffnagle, 2006; Svelto, 2010). We consider the case where the beam is at the focus point of the Gaussian beam, where $z = 0$. This enables us to simplify the equations (51) and (52):

$$w(0) = w_0 \tag{54}$$

$$I(r, 0) = I_{max} \exp\left(-2\left(\frac{r}{w_0}\right)^{2g}\right). \tag{55}$$

Four different illumination profiles are considered in this work. Gaussian distributions with Gaussian order of 1 (Normal Gaussian), super-Gaussian order of 4, super-Gaussian order of 16, and a fully uniform distribution. Figure 19 has these profiles visualized from the top and side views. Normal Gaussian distribution is the common output for single-mode fibers (Hui & O'Sullivan, 2008) and is preferred for free space power beaming due to its minimal divergence (Parent et al., 1992). Super-Gaussian distributions on the other hand are common output profiles for multimode fibers (Thorlabs). Multimode fibers are also preferable in high-power PbL systems, due to the higher powers they can transfer with their wider fiber cores (Vázquez et al., 2019). Lastly, uniform distribution acts as a reference for the optimal illumination profile to study the effects of nonuniform illumination. Uniform illumination can also occur in special systems consisting of cell matrices.
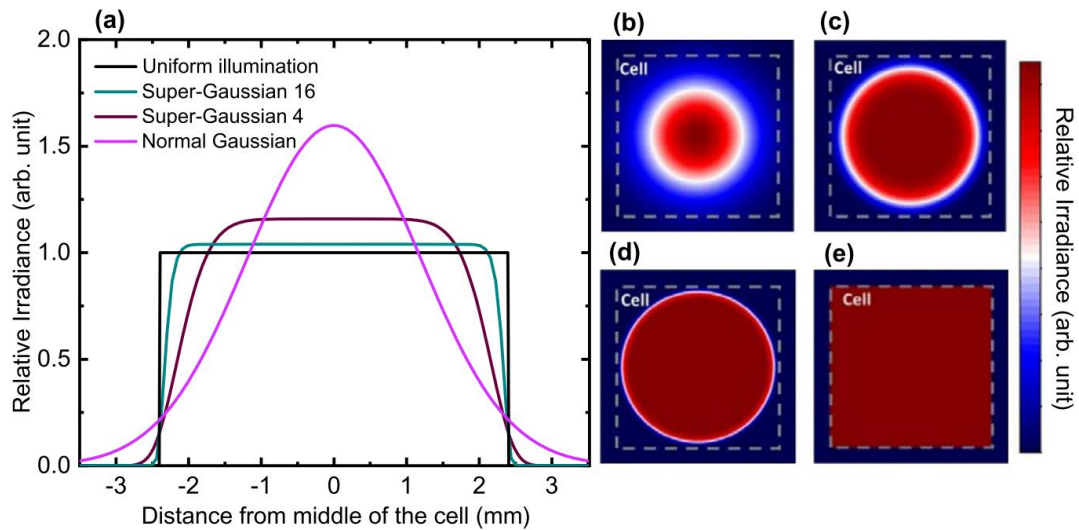

Figure 19 Top (a) and side view of the illumination profiles of Normal Gaussian (b), super-Gaussian 4 (c), super-Gaussian 16 (d), and uniform (e). (Nikander et al., 2021). Use under CC 4.0.

An optimal value for the beam waist to the given structures is calculated with the Hybrid quasi-3D model under 808 nm laser light and 40 W/cm² irradiance at 300 K. Figure 20 shows the simulation results. HQ3D model predicts a significant difference in the optimal beam waist values between the p–n and n–p structures, where p–n favours wider values and the n–p counterpart thinner. Also, the tolerance to use a smaller beam is smaller in the n–p polarity compared to the p–n structure.
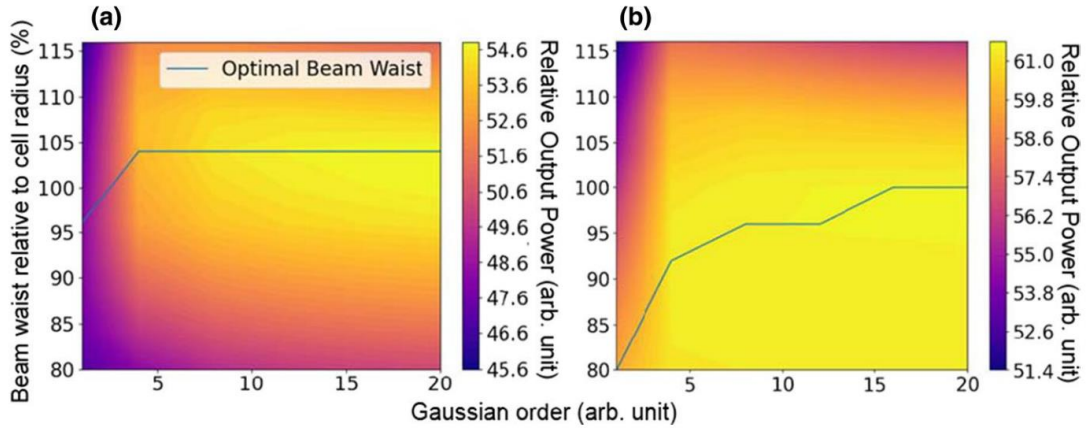
Figure 20 *Effect of size and shape of Gaussian beam to PV converter output power for (a) p–n and (b) n–p structures.* (Nikander et al., 2021)*. Use under CC 4.0.*

4.3 Grid optimization results

With the optimized illumination profiles, we can move to the grid optimization of our PV structures. The key optimization parameter for the double busbar finger grid is the spacing between the fingers. HQ3D simulation is done for a range of spacing values, where the *I–V* curve is extracted and relative figures of merit: FF, I_{sc}, V_{oc} and P_{mpp} are determined for the given device setting. Output power is then plotted as a function of finger spacing for visual inspection of the pattern performance. Polynomial fit is done for the plot to extract the exact value of the optimal spacing from the discrete data. On top of simulating the absolute values for the optimal spacing, a more detailed analysis of the tolerances for these optimal values is provided to form a complete picture of the spacing behavior for the given structure.

Grid optimization is done at a high, but realistic average irradiance of 40 W/cm^2. A wavelength of 808 nm is used since it is one of the most common wavelengths for commercially available lasers. Grid optimization is done for the four different illumination profiles with all having beam waist of 2.4 mm i.e., 96 % of the device radius. Using the same beam waist, we can study the effect of uneven illumination easier. Based on the results from the previous chapter, a value of the 2.4 mm beam waist is chosen to yield compromise of varying optimal beam waist values. On top of the different illumination profiles, simulation is also done for three different temperatures, 300 K, 325 K and 350 K. 300 K is used for comparability to common solar cell standard test conditions (The International Electrotechnical Commission, 2014) 325 K is a realistic operating temperature for a converter of this power level, and lastly 350 K is a more pessimistic case if the chip is used in higher ambient temperatures for example. Simulation results are shown as a spacing-

output power plot with the polynomial fit in Figure 21 and optimal spacings extracted with the polynomial fit are listed in Tables 2, 3, and 4.

The characteristic shape of the spacing-output power plots for p–n and n–p structures are considerably different regardless of the operating temperature and illumination profile. With both variants output power decreases as the finger spacing converges towards zero. This is somewhat trivial case, since zero spacing means full metal coverage on top of the cell. Full coverage maximizes the shading loss and effectively no light gets inside the converter cell. At larger spacing values, on the other hand, noticeable differences arise. After around 30 µm, the p–n structure's output power decreases substantially for all the simulated illuminations and temperatures. With the n–p structure, the output power starts also to decrease over 50 µm spacings, but the loss of power is much lower.

Another difference between the device polarities is the maximum power levels. For all cases roughly a 10 % increase in the output power is expected for the n–p structure over the p–n counterpart. Another key factor for the output power is the device temperature. Higher temperatures yield lower output powers which can be explained by the decrease of V_{oc} by temperature and subsequent decrease in output power.

Normal Gaussian distribution has noticeably lower output powers compared to the other illuminations. This is due to the "wide" shape of Normal Gaussian distribution compared to more confined profiles of super-Gaussian distributions, resulting 7.3 % leak of the illumination power outside the PV converter cell. This is considerably higher leaking compared to the next worse case of super-Gaussian of order 4, which has 0.1 % leaking out of the incident light.
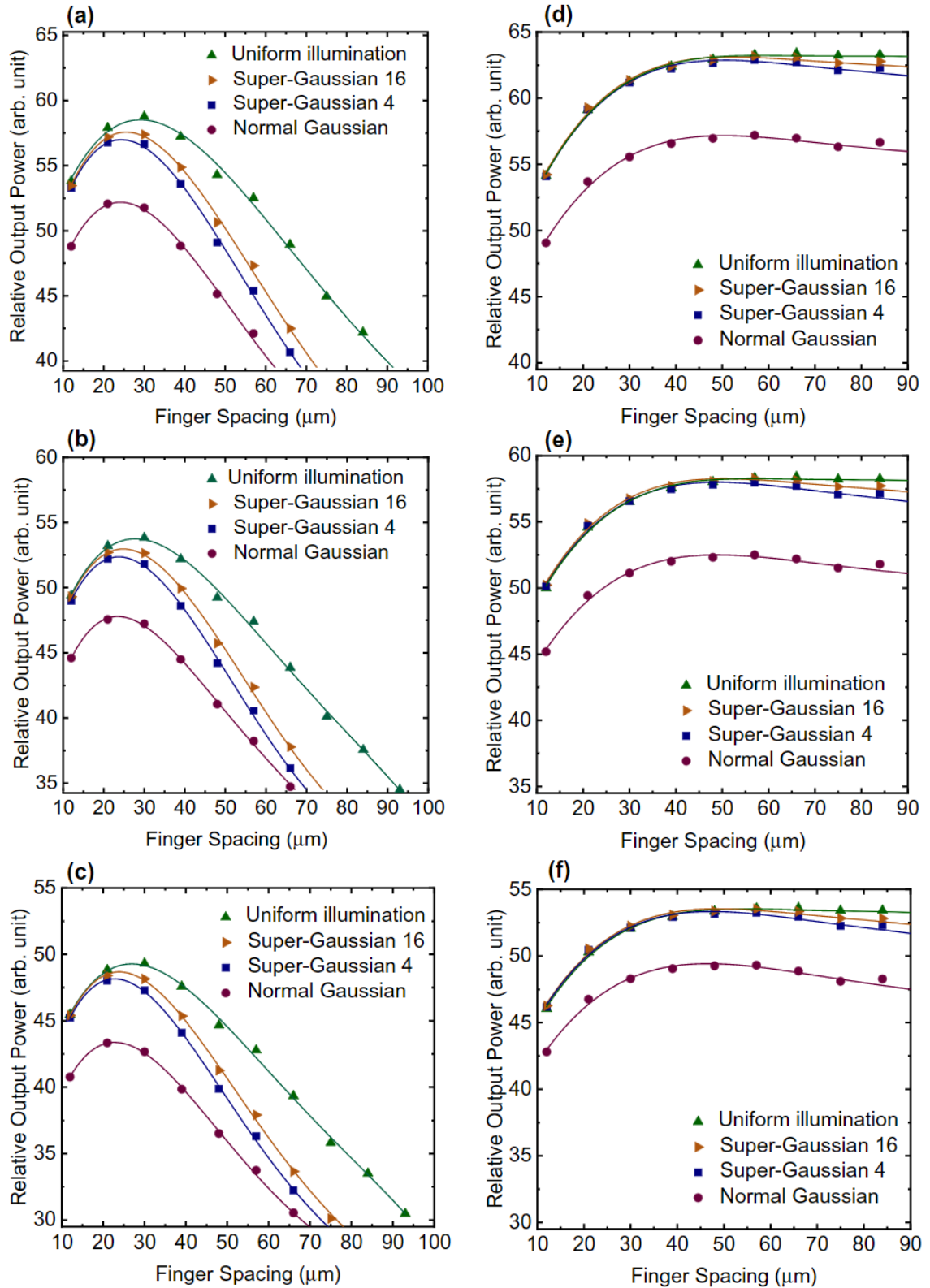
Figure 21 *HQ3D simulation results for relative output power as a function of finger spacing for p–n structure at (a) 300 K, (b) 325 K, and (c) 350 K and for n–p structure at (d) 300K, (e) 325 K, and (f) 350 K. Solid lines are the polynomial fit employed to extract the optimal spacing values.* (Nikander et al., 2021). *Use under CC 4.0.*

Table 2 *Optimal spacing values extracted by polynomial fit for p–n structure.*

Temperature (K)	Normal Gaussian (µm)	Super-Gaussian 4 (µm)	Super-Gaussian 16 (µm)	Uniform (µm)
300	24	25	26	29
325	24	24	25	28
350	23	23	24	27

Table 3 *Optimal spacing values extracted by polynomial fit for n–p structure.*

Temperature (K)	Normal Gaussian (µm)	Super-Gaussian 4 (µm)	Super-Gaussian 16 (µm)	Uniform (µm)
300	50	50	52	58
325	49	49	50	56
350	47	47	49	54

Table 4 *Maximum output powers (arb. unit) extracted by polynomial fit for p–n structure.*

Temperature (K)	Normal Gaussian	Super-Gaussian 4	Super-Gaussian 16	Uniform
300	52.2	57.0	57.6	58.5
325	47.7	52.4	53.0	53.8
350	43.4	48.2	48.7	49.3

Table 5 *Maximum output powers (arb. unit) extracted by polynomial fit for n–p structure.*

Temperature (K)	Normal Gaussian	Super-Gaussian 4	Super-Gaussian 16	Uniform
300	57.2	62.9	63.1	63.2
325	52.5	58.0	58.3	58.3
350	49.4	53.3	53.5	53.5

Optimal spacing and tolerance for getting 99 % of the output power is plotted as a function of temperature in Figure 22 and Figure 23. Tolerance values are tabulated in Table 6 and Table 7.

Table 6 *Tolerance of spacing values for getting 99 % of the maximum output power for p–n structure.*

Illumination profile	300 K (µm)	325 K (µm)	350 K (µm)
Normal	10	10	10
Gaussian	11	10	9
Super-Gaussian 4	11	11	10
Super-Gaussian 16	14	13	12

Table 7 *Tolerance of spacing values for getting 99 % of the maximum output power for n–p structure.*

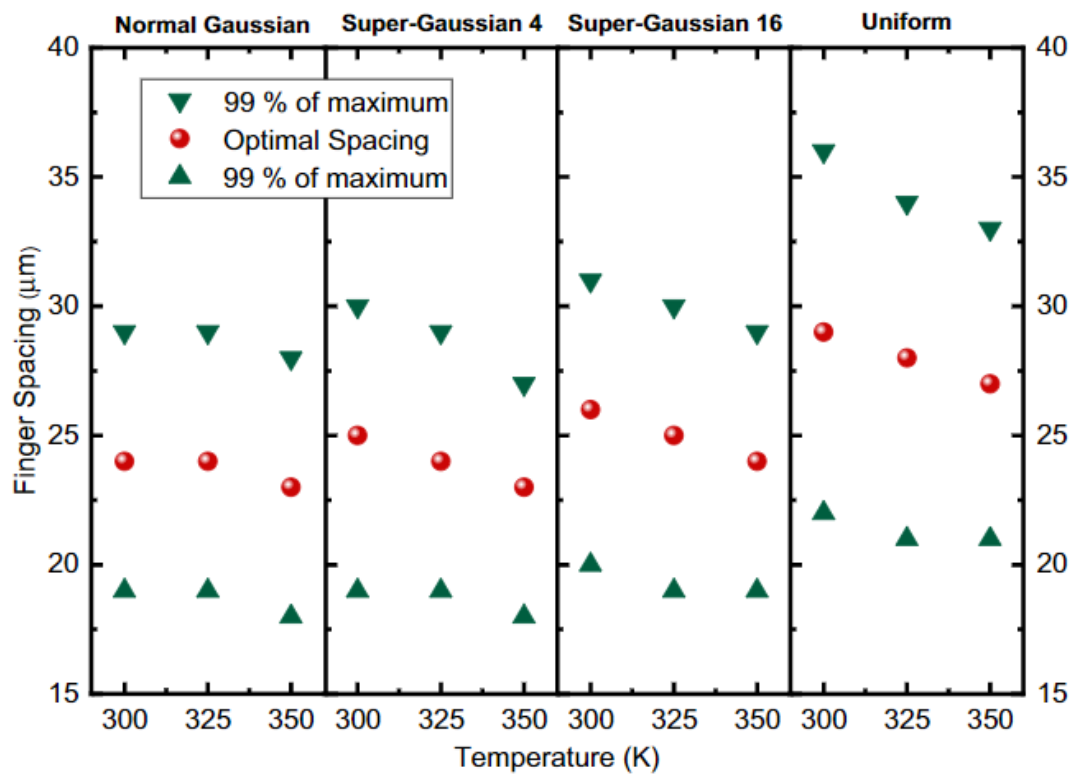| Illumination profile	300 K (µm)	325 K (µm)	350 K (µm)
Normal	34	31	27
Gaussian	37	32	30
Super-Gaussian 4	48	39	35
Super-Gaussian 16	64	63	61

Figure 22 *Optimal spacing values and tolerance for getting 99 % of the maximum output power as a function of temperature for p–n structure.* (Nikander et al., 2021). *Use under CC 4.0.*

Figure 23 *Optimal spacing values and tolerance for getting 99 % of the maximum output power as a function of temperature for n–p structure.* (Nikander et al., 2021). *Use under CC 4.0.*
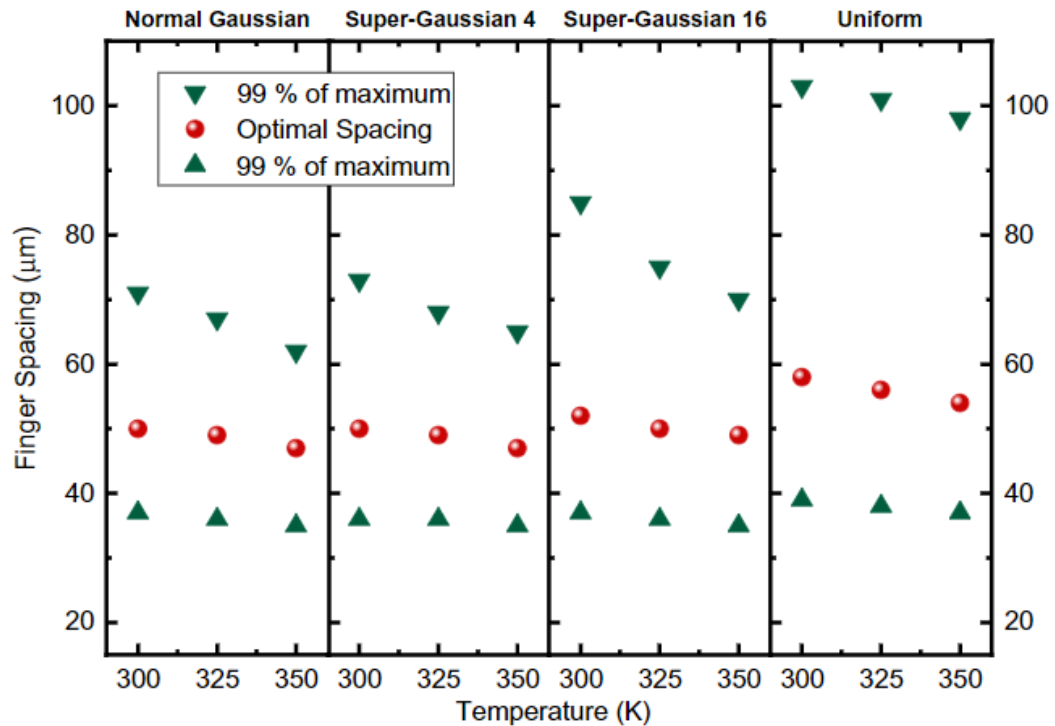
Spacing tolerance for the p–n structure is considerably lower compared to the n–p structure. With both structures, tolerances increase when beam uniformity increases. This effect is much more substantial with the n–p structure.

Whereas with the p–n structure, tolerances are slightly increased with beam uniformity, beam uniformity has a slight positive relation with increased tolerances, this effect is considerably increased with the n–p structure. Also, the increasing operating temperature has a negative effect to the spacing tolerances, which is amplified at the higher tolerance n–p structure.

Optimal spacing has a slight, linear-like, downward trend as the device temperature is increased. This is explained by the increase in resistivity of gold as the temperature is increased. With higher resistivity, more gold needs to be added to compensate for the resistivity, yielding narrower spacing. Increased temperature also lowers tolerances for nearly all of the studied cases, except for p–n structure at 300 K and Normal Gaussian illumination, where the tolerance stays at a constant 10 µm.

5. ANALYSIS

The previous chapter analyzed the behavior of the output power and its relation to varying spacing values. From equation (9) we know that output power can be divided into photovoltaic performance factors: I_{sc}, FF, and V_{oc}. With these factors, we seek to gain a deeper understanding of the physical effects influenced by the metal contacts, illumination, and temperature. I_{sc}, FF, and V_{oc} are plotted in Figure 24, Figure 25, and Figure 26 respectively for the case of 300 K. We see that the I_{sc} decreases as the spacing gets smaller for the whole data set. This is explained by the increase of shading loss induced by the increased area covered by the front metallization pattern. The decrease in I_{sc} at narrow spacing also reflects the decrease in output power when moving to lower spacing values.
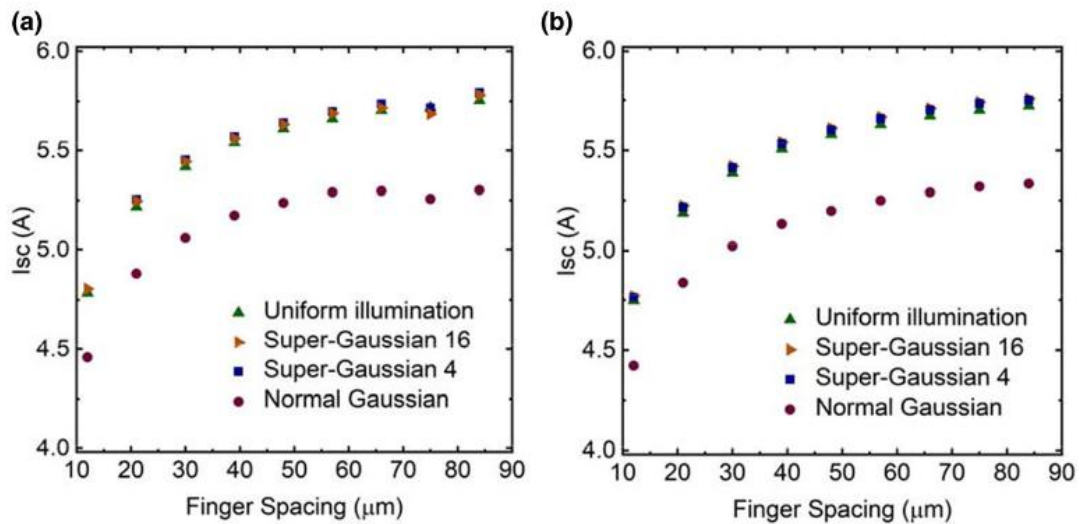

Figure 24 *Short circuit current as a function of finger spacing for (a) p–n structure (b) n–p structure at 300 K.* (Nikander et al., 2021). *Use under CC 4.0.*

The FF results reveal the reason for differences in spacing-output power plots. Whereas the n–p structure enjoys the low sheet resistance and thus does not need much front metallization in aiding the current at the lateral direction, p–n counterpart suffers from the poor sheet resistances induced by low majority carrier mobility. This results in comparably higher resistive losses, which manifest in reduced FF. Figure 25 (a) showcases nicely the importance of front contact metallization in cases of reducing the resistive losses of PV devices. Especially in multijunction designs, the layer thicknesses are often thinner (Luque & Hegedus, 2010), and thus large sheet resistances are realized.

From Figure 25 (a) we also see that the FF of uniform illumination profile stays higher as spacing is increased in the p–n structure. This further highlights the importance of uniformity of illumination in high irradiance applications. The reason for this difference is due to the higher current densities at the peak of the illumination profile, creating more resistive losses.
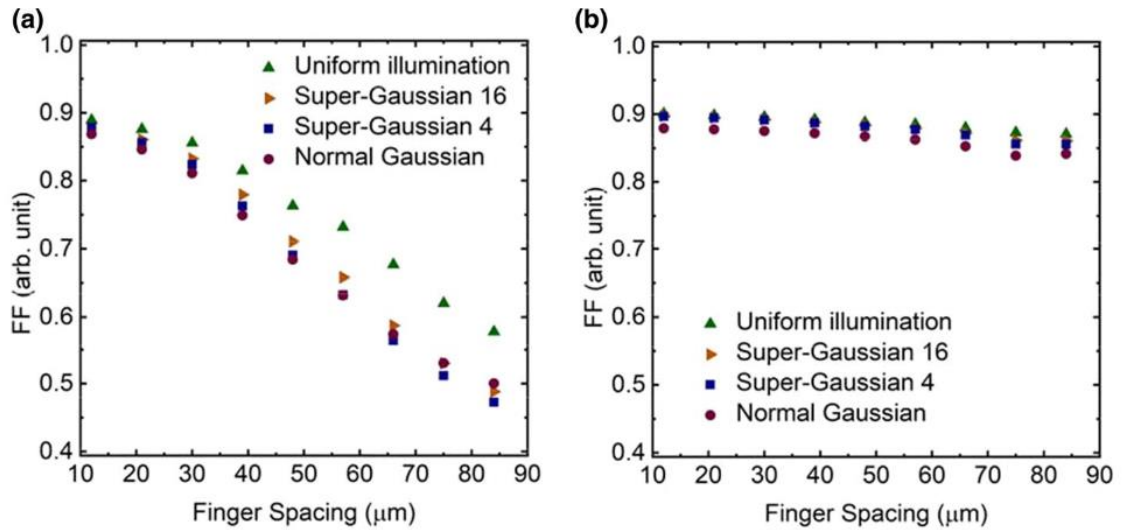

Figure 25 *Fill factor as a function of finger spacing for (a) p–n structure (b) n–p structure at 300 K.* (Nikander et al., 2021)*. Use under CC 4.0.*
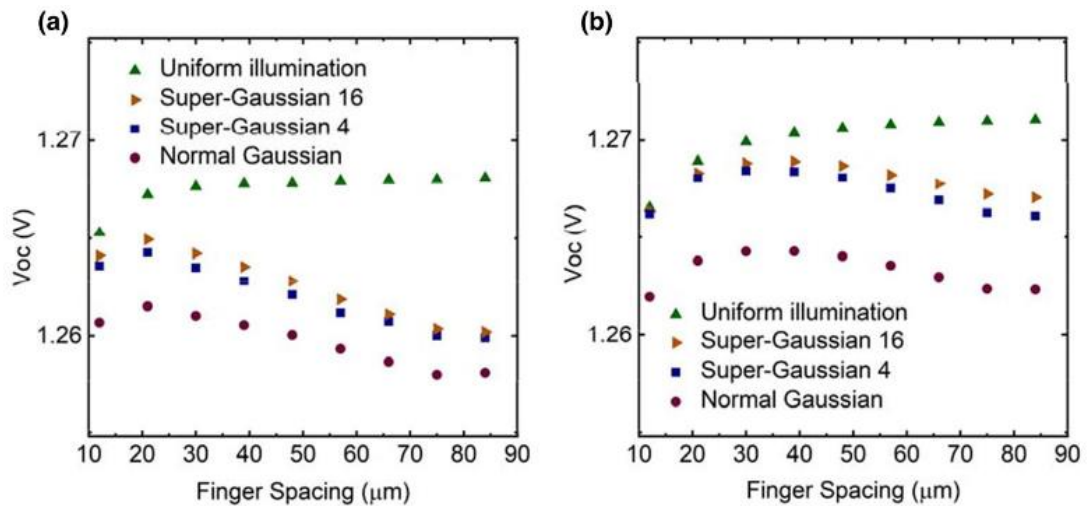

Figure 26 *Open circuit voltage as a function of finger spacing for (a) p–n structure (b) n–p structure at 300 K.* (Nikander et al., 2021)*. Use under CC 4.0.*

Results for the V_{oc} as a function of finger spacing reveal another interesting effect of uneven illumination. Contrary to PV theory (Luque & Hegedus, 2010), V_{oc} values are decreasing with larger spacing values for uneven illumination even though the I_{sc} increases. The uniform beam still behaves as expected, so this decrease in V_{oc} has to come from

the non-uniformity of the illumination. This reduction in V_{oc} can be explained by laterally uneven voltage generation over the junction resulting from the uneven illumination. One can think the cell to consist of multiple small parallelly connected cells or in this case voltage sources, which all have different voltages. Cells at the corners of the cell, with low illumination, will produce smaller voltage than cells at the peak of the illumination profile. As the open circuit voltage of a photovoltaic cell is exponentially related to photogenerated current, cells getting less illumination lose more voltage than cells with increased illumination gain. This effect will lead to decreased V_{oc} values in uneven illumination. At the same time, the structure tries to equalize this lateral potential difference, but as the spacing is decreased i.e., lateral resistance increases, this equalization can't be done as effectively. This results in the decrease of V_{oc} with the increase of spacing.

6. CONCLUSION

In this thesis novel quasi-3D simulation framework, Hybrid quasi-3D model has been developed based on existing photovoltaics simulation models and tools of the transfer matrix method, Poisson-drift-diffusion model, double diode model and quasi-3D model. HQ3D model was deployed on Python coding language and the backbone of the tool was Solcore, a Python library for modelling solar cells and semiconductor materials.

Two photovoltaic converters with a single junction design were simulated. One of a p–n polarity structure and a similar inverted n–p counterpart was considered. Extensive simulations were done for these cell structures with the emphasis on metal front contact grid pattern optimization of the two-busbar finger grid pattern. Optimization was done by doing HQ3D simulations for a range of finger spacings values and fitting a polynomial fit to the simulation's output power results. Grid optimization was done for three temperatures of 300 K, 325 K and 350 K and four illumination profiles of uniform, Normal Gaussian, and two super-Gaussian distributions.

Simulations predicted that the n–p structure would yield considerably higher output powers in all the simulated cases when compared to the p–n counterpart. This result was somehow expected due to the substantially higher sheet resistance of the emitter layer of the p–n design. The simulation yielded also much wider spacings for the n–p structure, them being roughly double for the spacings of the p–n structure.

Illumination profile was also found to have effects on optimal spacing and output power. A less uniform profile of Normal Gaussian distribution yielded 10-20 % narrower spacing compared to the fully unform case. With Normal Gaussian distribution, output powers were decreased due to the light not being confined to the cell area. With slightly more confined distributions of super-Gaussian 4 and 16, leaking decreased to negligible amounts of loss of about 0.1 %. Temperature was also found to decrease spacing, which was expected due to the increase in resistance of contact metallization.

On top of absolute spacing values, also spacing tolerances for desired 99 % of the maximum power of the optimal spacing were calculated and analysed. Here too, the n–p structure outperformed between the two designs yielding three to five times larger tolerances when compared to the p–n structure. Both temperature and beam uniformity was found to decrease the spacing tolerances with a more profound decrease occurring with the decrease in beam uniformity.

Further analysis of the photovoltaic output power performance factors: I_{sc}, FF, and V_{oc} was also done. FF results revealed the high resistive losses at p–n structure with increased spacing. When compared to FF results of n–p structure, one can determine, that the low majority carrier mobility for p–type GaAs compared to n–type GaAs, the consequently high layer sheet resistance of the emitter layer has a detrimental effect on the p–n design at high power density applications. Thus, this work concludes that n–p designs should be favored over p–n designs in high power ≥ 40 W/m² applications whenever possible.

Another interesting discovery of this work was the slight decrease in V_{oc} with the increase of finger spacing with uneven illumination. This contradiction with the general observation of V_{oc} increasing with increased photogenerated current was explained with a thought experiment on parallelly connected voltage sources trying to equalize their potentials.

This work also has contributed to the field of photovoltaic device simulation, by developing a combined simulation tool, Hybrid quasi-3D model, from established, rigorous but efficient models. The model proved its capabilities in complex, multi-variable simulation tasks. As such tool is an excellent addition to photovoltaic scientist's and especially engineer's tool kit. By being able to simultaneously optimize spacing, illumination and device structures, can the development work take the next step from chip level to module level design.

This thesis focused on optimizing the front contact grid spacing. A natural next step for this work would be to expand the HQ3D simulations for studying various tolerance parameters of the illumination profile, such as displacement, beam size and beam angle. Also optimizing the underlaying photovoltaic structure for given illumination and grid designs is of high interest for the author.

REFERENCES

Alonso-Álvarez, D., & Ekins-Daukes, N. (2016). SPICE Modelling of Photoluminescence and Electroluminescence Based Current-Voltage Curves of Solar Cells for Concentration Applications. *Journal of Green Engineering*, *5*(4), 33–48. https://doi.org/10.13052/jge1904-4720.5343

Alonso-Álvarez, D., Wilson, T., Pearce, P., Führer, M., Farrell, D., & Ekins-Daukes, N. (2018). Solcore: a multi-scale, Python-based library for modelling solar cells and semiconductor materials. *Journal of Computational Electronics*, *17*(3), 1099–1123. https://doi.org/10.1007/s10825-018-1171-3

Ameri, T., Li, N., & Brabec, C. J. (2013). Highly efficient organic tandem solar cells: A follow up review. In *Energy and Environmental Science* (Vol. 6, Issue 8, pp. 2390–2413). https://doi.org/10.1039/c3ee40388b

ASTM International. (2019). *Standard Solar Constant and Zero Air Mass Solar Spectral Irradiance Tables*. https://www.astm.org/e0490-00ar19.html

ASTM International. (2020). *Standard Tables for Reference Solar Spectral Irradiances: Direct Normal and Hemispherical on 37° Tilted Surface*. https://www.astm.org/g0173-03r20.html

Bartek, M., Correia, J. H., & Wolffenbuttel, R. F. (1999). Silver-based reflective coatings for micromachined optical filters. *Journal of Micromechanics and Microengineering*, *9*(2), 162–165. https://doi.org/10.1088/0960-1317/9/2/314

Benamira, A., & Pattanaik, S. (2020). Application of the Transfer Matrix Method to Anti-reflective Coating Rendering. *Lecture Notes in Computer Science (Including Subseries Lecture Notes in Artificial Intelligence and Lecture Notes in Bioinformatics)*, *12221 LNCS*, 83–95. https://doi.org/10.1007/978-3-030-61864-3_8

Bouclé, J., Ribeiro Dos Santos, D., & Julien-Vergonjanne, A. (2023). Doing More with Ambient Light: Harvesting Indoor Energy and Data Using Emerging Solar Cells. *Solar*, *3*(1), 161–183. https://doi.org/10.3390/solar3010011

Brown, A. S., & Green, M. A. (2002). Limiting efficiency for current-constrained two-terminal tandem cell stacks. *Progress in Photovoltaics: Research and Applications*, *10*(5), 299–307. https://doi.org/10.1002/pip.425

Byrnes, S. J. (2016). *Multilayer optical calculations*. http://arxiv.org/abs/1603.02720

Chetvorno. (2017). *File:Solid state electronic band structure.svg - Wikimedia Commons*. https://commons.wikimedia.org/wiki/File:Solid_state_electronic_band_structure.svg

Corless, R. M., Gonnet, G. H., Hare, D. E. G., Jeffrey, D. J., & Knuth, D. E. (1996). On the Lambert W function. *Advances in Computational Mathematics*, *5*(1), 329–359. https://doi.org/10.1007/bf02124750

Datas, A., López-Ceballos, A., López, E., Ramos, A., & del Cañizo, C. (2022). Latent heat thermophotovoltaic batteries. *Joule*, *6*(2), 418–443. https://doi.org/10.1016/j.joule.2022.01.010

De Nazaré, F. V. B., & Werneck, M. M. (2012). Hybrid optoelectronic sensor for current and temperature monitoring in overhead transmission lines. *IEEE Sensors Journal*, *12*(5), 1193–1194. https://doi.org/10.1109/JSEN.2011.2163709

DeLoach, B. C., Miller, R. C., & Kaufman, S. (1978). Sound Alerter Powered Over an Optical Fiber. *Bell System Technical Journal*, *57*(9), 3309–3316. https://doi.org/10.1002/j.1538-7305.1978.tb02205.x

Fafard, S., & Masson, D. P. (2021). Perspective on photovoltaic optical power converters. In *Journal of Applied Physics* (Vol. 130, Issue 16, p. 160901). American Institute of Physics Inc. https://doi.org/10.1063/5.0070860

Gao, X., Cui, Y., Hu, J., Xu, G., & Yu, Y. (2016). Lambert W-function based exact representation for double diode model of solar cells: Comparison on fitness and parameter extraction. *Energy Conversion and Management*, *127*, 443–460. https://doi.org/10.1016/j.enconman.2016.09.005

Geisz, J. F., France, R. M., Schulte, K. L., Steiner, M. A., Norman, A. G., Guthrey, H. L., Young, M. R., Song, T., & Moriarty, T. (2020). Six-junction III–V solar cells with 47.1% conversion efficiency under 143 Suns concentration. *Nature Energy*, *5*(4), 326–335. https://doi.org/10.1038/s41560-020-0598-5

Gonzalez-Pedro, V., Juarez-Perez, E. J., Arsyad, W. S., Barea, E. M., Fabregat-Santiago, F., Mora-Sero, I., & Bisquert, J. (2014). General working principles of CH3NH3PbX3 perovskite solar cells. *Nano Letters*, *14*(2), 888–893. https://doi.org/10.1021/nl404252e

Green, M. A., Dunlop, E. D., Hohl-Ebinger, J., Yoshita, M., Kopidakis, N., & Hao, X. (2021). Solar cell efficiency tables (Version 58). *Progress in Photovoltaics: Research and Applications*, *29*(7), 657–667. https://doi.org/10.1002/pip.3444

Gupta, D. K., Langelaar, M., Barink, M., & van Keulen, F. (2016). Optimizing front metallization patterns: Efficiency with aesthetics in free-form solar cells. *Renewable Energy*, *86*, 1332–1339. https://doi.org/10.1016/j.renene.2015.09.071

Hazewinkel, M. (1995). Encyclopaedia of Mathematics. In *Encyclopaedia of Mathematics*. Springer US. https://doi.org/10.1007/978-1-4899-3791-9

Hong, H. F., Huang, T. S., & Chen, Y. Y. (2014a). Influence of metal grid spacing on the conversion efficiency of concentration solar cell at different illumination levels. *Materials Science and Engineering B: Solid-State Materials for Advanced Technology*, *188*, 43–47. https://doi.org/10.1016/j.mseb.2014.05.011

Hong, H. F., Huang, T. S., & Chen, Y. Y. (2014b). Influence of metal grid spacing on the conversion efficiency of concentration solar cell at different illumination levels. *Materials Science and Engineering B: Solid-State Materials for Advanced Technology*, *188*, 43–47. https://doi.org/10.1016/j.mseb.2014.05.011

Hui, R., & O'Sullivan, M. (2008). Fiber Optic Measurement Techniques. In *Fiber Optic Measurement Techniques*. Elsevier. https://doi.org/10.1016/B978-0-12-373865-3.X0001-8

Huo, P., & Rey-Stolle, I. (2017). Al-based front contacts for HCPV solar cell. *AIP Conference Proceedings*, *1881*(1), 040004. https://doi.org/10.1063/1.5001426

IEA. (2022). *Solar PV – Analysis*. https://www.iea.org/reports/solar-pv

IEA-PVPS. (2022). *Trends in PV Applications 2022*. https://iea-pvps.org/trends_reports/trends-2022/

Johnson, P. B., & Christy, R. W. (1972). Optical constants of the noble metals. *Physical Review B*, *6*(12), 4370–4379. https://doi.org/10.1103/PhysRevB.6.4370

Jošt, M., Kegelmann, L., Korte, L., & Albrecht, S. (2020). Monolithic Perovskite Tandem Solar Cells: A Review of the Present Status and Advanced Characterization Methods Toward 30% Efficiency. In *Advanced Energy Materials* (Vol. 10, Issue 26). Wiley-VCH Verlag. https://doi.org/10.1002/aenm.201904102

Lide, D. R. (1997). *Handbook of Chemistry and Physics* (75th ed.). CRC Press.

Lopez-Cardona, J. D., Altuna, R., Montero, D. S., & Vazquez, C. (2021). Power over Fiber in C-RAN with Low Power Sleep Mode Remote Nodes Using SMF. *Journal of Lightwave Technology*, *39*(15), 4951–4957. https://doi.org/10.1109/JLT.2021.3080631

Luque, A., & Hegedus, S. (2010). Handbook of Photovoltaic Science and Engineering. In A. Luque & S. Hegedus (Eds.), *Handbook of Photovoltaic Science and Engineering*. Wiley. https://doi.org/10.1002/9780470974704

Nelder, J. A., & Mead, R. (1965). A Simplex Method for Function Minimization. *The Computer Journal*, *7*(4), 308–313. https://doi.org/10.1093/comjnl/7.4.308

Ngspice, the open source Spice circuit simulator - Intro. (n.d.). Retrieved October 1, 2020, from http://ngspice.sourceforge.net/

Nikander, V. (2020). *III-V-PUOLIJOHDEAURINKOKENNOJEN MALLINNUS DIODIYHTÄLÖLLÄ*. https://trepo.tuni.fi/handle/10024/122067

Nikander, V., Wei, J., Aho, A., Polojarvi, V., Tukiainen, A., & Guina, M. (2021). Hybrid quasi-3D optimization of grid architecture for single junction photovoltaic converters. *Optical and Quantum Electronics*, *53*(4), 205. https://doi.org/10.1007/s11082-021-02850-x

Oliva, E., Dimroth, F., & Bett, A. W. (2008). GaAs converters for high power densities of laser illumination. *Progress in Photovoltaics: Research and Applications*, *16*(4), 289–295. https://doi.org/10.1002/pip.811

Parent, A., Morin, M., & Lavigne, P. (1992). Propagation of super-Gaussian field distributions. *Optical and Quantum Electronics*, *24*(9), S1071–S1079. https://doi.org/10.1007/BF01588606

Python.org. (n.d.). *About Python^{TM} | Python.org*. Retrieved March 21, 2023, from https://www.python.org/about/

Reichmuth, S. K., Helmers, H., Philipps, S. P., Schachtner, M., Siefer, G., & Bett, A. W. (2017). On the temperature dependence of dual-junction laser power converters. *Progress in Photovoltaics: Research and Applications*, *25*(1), 67–75. https://doi.org/10.1002/pip.2814

Riede, M., Spoltore, D., & Leo, K. (2021). Organic Solar Cells—The Path to Commercial Success. *Advanced Energy Materials*, *11*(1). https://doi.org/10.1002/aenm.202002653

Serway, R. A., & Jewett, J. W. (2006). *Serway's Principles of Physics: A Calculus-based Text*. Thomson Brooks/Cole.

Shabat, M. M., El-Khozondar, H. J., Alshembari, A. A., & El-Khozondar, R. J. (2018). Transfer matrix method application on semiconductor-based solar cell characteristics measurements. *Modern Physics Letters B*, *32*(28). https://doi.org/10.1142/S0217984918503463

Shealy, D. L., & Hoffnagle, J. A. (2006). Laser beam shaping profiles and propagation. *Applied Optics*, *45*(21), 5118–5131. https://doi.org/10.1364/AO.45.005118

Software Spectra Inc. (2008). Optical Data from Sopra S. A.

Sotoodeh, M., Khalid, A. H., & Rezazadeh, A. A. (2000). Empirical low-field mobility model for III-V compounds applicable in device simulation codes. *Journal of Applied Physics*, *87*(6), 2890–2900. https://doi.org/10.1063/1.372274

Streetman, B., & Banerjee, S. (2015). *Solid State Electronic Devices, Global Edition* [Book]. Pearson Education, Limited.

Svelto, O. (2010). Principles of lasers. In *Principles of Lasers*. Springer US. https://doi.org/10.1007/978-1-4419-1302-9

Sze, S. M., & Irvin, J. C. (1968). Resistivity, mobility and impurity levels in GaAs, Ge, and Si at 300°K. *Solid State Electronics*, *11*(6), 599–602. https://doi.org/10.1016/0038-1101(68)90012-9

The International Electrotechnical Commission. (2014). International standard IEC 60904–08, edition 3.0, 2014–05, photovoltaic devices—part 8: measurement of spectral responsivity of a photovoltaic (pv) device. *Technical Report The International Electrotechnical Commission (IEC)*.

Thorlabs. (n.d.). *Multimode Fiber Beam Profiles Lab Facts*. Retrieved March 9, 2023, from https://www.thorlabs.com/newgrouppage9.cfm?objectgroup_id=11993

Tong, Y., Xiao, Z., Du, X., Zuo, C., Li, Y., Lv, M., Yuan, Y., Yi, C., Hao, F., Hua, Y., Lei, T., Lin, Q., Sun, K., Zhao, D., Duan, C., Shao, X., Li, W., Yip, H. L., Xiao, Z., … Ding, L. (2020). Progress of the key materials for organic solar cells. In *Science China Chemistry* (Vol. 63, Issue 6, pp. 758–765). Science in China Press. https://doi.org/10.1007/s11426-020-9726-0

Vänttinen, K., Lammasniemi, J., Rakennus, K., Asonen, H., Jurva, R., & Karioja, P. (1995). A Ga0.51In0.49P/GaAs-based photovoltaic converter for two-directional optical power and data transmission. *Progress in Photovoltaics: Research and Applications*, *3*(1), 57–63. https://doi.org/10.1002/pip.4670030107

Varshni, Y. P. (1967). Temperature dependence of the energy gap in semiconductors. *Physica*, *34*(1), 149–154. https://doi.org/10.1016/0031-8914(67)90062-6

Vázquez, C., López-Cardona, J. D., Lallana, P. C., Montero, D. S., Al-Zubaidi, F. M. A., Pérez-Prieto, S., & Pérez Garcilópez, I. (2019). Multicore Fiber Scenarios Supporting Power over Fiber in Radio over Fiber Systems. *IEEE Access*, *7*, 158409–158418. https://doi.org/10.1109/ACCESS.2019.2950599

Vinod, P. N. (2008). Power loss calculation as a reliable methodology to assess the ohmic losses of the planar ohmic contacts formed on the photovoltaic devices. *Journal of Materials Science: Materials in Electronics*, *19*(7), 594–601. https://doi.org/10.1007/s10854-007-9395-1

Vurgaftman, I., Meyer, J. R., & Ram-Mohan, L. R. (2001). Band parameters for III-V compound semiconductors and their alloys. *Journal of Applied Physics*, *89*(11 I), 5815–5875. https://doi.org/10.1063/1.1368156

Wang, D., Wright, M., Elumalai, N. K., & Uddin, A. (2016). Stability of perovskite solar cells. In *Solar Energy Materials and Solar Cells* (Vol. 147, pp. 255–275). Elsevier. https://doi.org/10.1016/j.solmat.2015.12.025

Ward, J. S., Duda, A., Friedman, D. J., Geisz, J., McMahon, W., & Young, M. (2015). High aspect ratio electrodeposited Ni/Au contacts for GaAs-based III-V concentrator solar cells. *Progress in Photovoltaics: Research and Applications*, *23*(5), 646–653. https://doi.org/10.1002/pip.2490

Yeh, P. (2005). *Optical Waves in Layered Media*. Wiley.